Click Here for Full Article

Rheological controls on the terrestrial core formation mechanism

G. J. Golabek

Geophysical Fluid Dynamics, Institute of Geophysics, ETH Zurich, CH–8092 Zurich, Switzerland (gregor.golabek@erdw.ethz.ch)

T. V. Gerya

Geophysical Fluid Dynamics, Institute of Geophysics, ETH Zurich, CH–8092 Zurich, Switzerland (taras.gerya@erdw.ethz.ch)

Also at Department of Geology, Moscow State University, 119899 Moscow, Russia

B. J. P. Kaus

Geophysical Fluid Dynamics, Institute of Geophysics, ETH Zurich, CH–8092 Zurich, Switzerland (kaus@erdw.ethz.ch)

Also at Department of Earth Sciences, University of Southern California, 3651 Trousdale Parkway, Los Angeles, California 90089, USA

R. Ziethe

European Space Research and Technology Centre, European Space Agency, NL–2201 AZ Noordwijk ZH, Netherlands (rziethe@rssd.esa.int)

P. J. Tackley

Geophysical Fluid Dynamics, Institute of Geophysics, ETH Zurich, CH–8092 Zurich, Switzerland (paul.tackley@erdw.ethz.ch)

[1] Iron core differentiation of terrestrial planetary bodies is thought to have occurred simultaneously with planetary accretion. The exact mechanisms of core formation, however, remain incompletely understood. One model proposes that cores are formed from numerous smaller iron cores from predifferentiated planetesimals. To further understand this mechanism for forming Mars- and Earth-sized bodies, we present here systematic numerical simulations. Our models include a non-Newtonian temperature-, pressure- and strain rate–dependent viscoplastic rheology. Four different core formation regimes are being observed in the study, as a function of activation volume, friction angle, Peierls stress, and the initial temperature state of the body. We derive scaling laws, which show the importance of shear heating localization and plastic yielding as mechanisms to drive planetary differentiation in planetary interiors, that are in good agreement with numerical simulations. Results indicate that the effective rheology of the planetary body has a major effect on the core formation mechanism: while bodies with a weak rheology generally show a diapiric mode of core formation, the interior of planetary bodies with a stiff rheology can be fractured or displaced toward the surface. On Earth-sized protoplanets, the water content seems also to have a significant influence on the mode of core formation. Results indicate a time scale of differentiation of a few million years, significantly shorter than expected from the Stokes sinking time in a Newtonian medium.

1. Introduction

[2] While the existence of the Earth's core has been known for a long time [*Gutenberg*, 1913], knowledge about its formation mechanism is still very limited. Current understanding indicates that accretion and differentiation of larger terrestrial bodies took place simultaneously and lasted for about 100 Ma for the Earth (see the review by *Chambers* [2004, and references therein]). This is broadly consistent with isotopic data ranging from 70 to 110 Ma from short-lived chronometers [*Halliday*, 2008] to about 100 Ma estimated from long-lived radioactive isotopes [e.g., *Allègre et al.*, 2008]. Three sources have been proposed to deliver the energy required for significant melting in the early Earth: (1) decay of short-lived radioactive isotopes such as ^{26}Al [*MacPherson et al.*, 1995] ($t_{1/2}$ = 0.73 Ma) and the less prominent ^{60}Fe ($t_{1/2}$ = 1.5 Ma) (half-life times from *Carlson and Lugmair* [2000]), (2) impact heating by accreted planetesimals and planetary embryos [*Davies*, 1985; *Melosh*, 1990], and (3) impact associated gravitational unloading [*Asphaug et al.*, 2006]. Numerical models performed by *Merk et al.* [2002] show that a planetesimal with a radius of about 100 km heated by the radioactive decay of ^{26}Al can experience relatively high central temperatures. Depending on the concentration of radioactive isotopes, temperature values between 600 and over 2000 K have been proposed in the case of homogeneous accretion of a planetesimal. Thus, it would be possible to at least partially melt iron and predifferentiate early formed smaller bodies [*Greenwood et al.*, 2005; *Hevey and Sanders*, 2006; *Sahijpal et al.*, 2007; *Weiss et al.*, 2008; *Day et al.*, 2009] via a rainfall mechanism [*Stevenson*, 1990; *Rubie et al.*, 2003, 2007; *Höink et al.*, 2006] or through percolation [*Terasaki et al.*, 2008; *Yoshino et al.*, 2004] before short-lived radioactive isotopes become extinct (see Figure 1). Models of planetary formation indicate that the size of

impacting planetesimals increases with accretion time [e.g., *Wetherill*, 1990]. Thus, at a certain point, a sufficient amount of impact energy is converted into heat to allow the formation of melt at or near the surface of a growing planetary body. It has been suggested by several authors [*Sasaki and Nakazawa*, 1986; *Melosh*, 1990; *Tonks and Melosh*, 1992; *Senshu et al.*, 2002] that this stage is reached at the latest when a planetary embryo obtains about 10% of the present-day Earth mass (about the mass of today's Mars). This mass can be accumulated within 0.1–10 Ma [e.g., *Wetherill*, 1990; *Chambers*, 2004], assuming a runaway growth of the planetary embryos [e.g., *Kokubo and Ida*, 2000, and references therein]. Therefore, depending on the specific accretion time to reach Mars mass, the main body could have either cooled or stayed warm. This leads to a scenario in which core formation restarts after a possible early melting episode when the growing planetary embryo reaches about Mars mass (see Figure 1). Impacts then become energetic enough to generate a new magma ocean or magma ponds overlying a central region [see *Stevenson*, 1981, 1990; *Karato and Murthy*, 1997]. The magma ocean consists of molten chondritic material, i.e., a homogeneous mixture of molten silicates and iron. Support for the existence of a magma ocean comes from recent results by, e.g., *Wood et al.* [2008, and references therein], which indicate that today's mantle depletion of moderately and highly siderophile elements might be explained by the equilibration between metals and silicates in an intermediate-depth magma ocean. Again, the rainfall mechanism enables gravitational separation of molten silicates and iron, which leads to the formation of ponds or a complete layer of molten iron accumulated at the base of a magma ocean or at the bottom of large impact craters. Since the density of the overlying iron is higher than that of the central region of the early planetary embryo, Rayleigh-Taylor (RT) instabilities may form iron diapirs [e.g., *Ziethe*
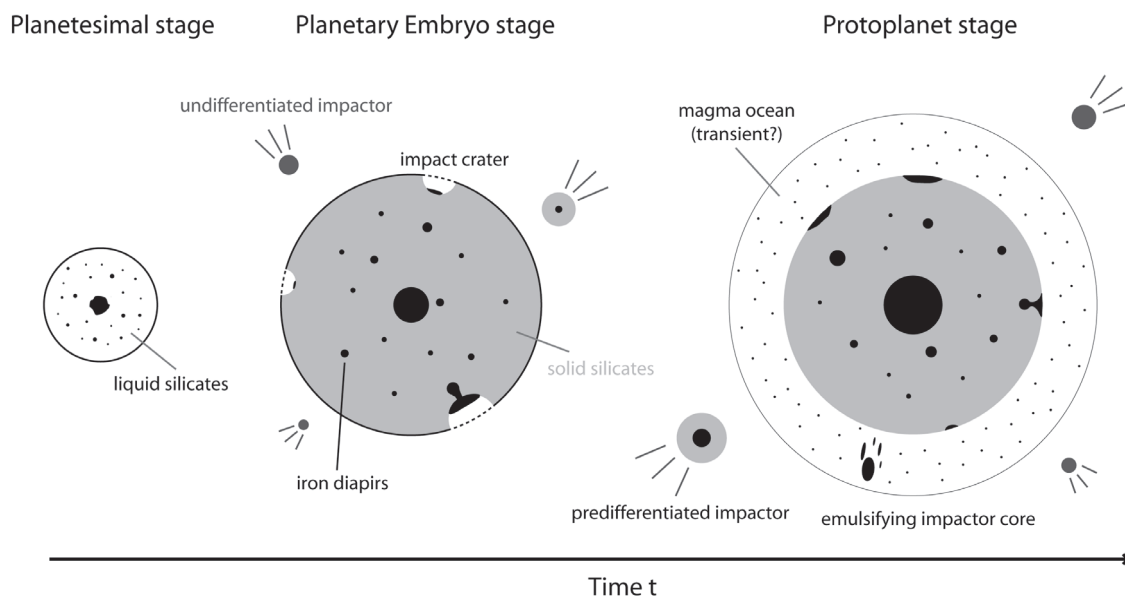
Figure 1. Sketch of core formation during planetary accretion.

and Spohn, 2007; *Samuel and Tackley*, 2008] or a large iron drop that displaces the central core in the sense of *Elsasser* [1963]. During this overturn process, stresses can become very large and fracture or deform the material in the central region so that it spreads as a mantle of "rockbergs" around the newly formed iron core [*Stevenson*, 1981; *Ida et al.*, 1987]. *Honda et al.* [1993] and recently *Lin et al.* [2009] modeled this scenario numerically, starting with an iron ring surrounding the central region of the planetary embryo. They showed that, depending on the viscosity of the central region and therefore also its temperature, it is possible to switch from the above mentioned overturn mechanism in a cold, stiff interior to a higher-temperature mode in which the iron core is formed by the sinking of many small iron diapirs. Thus, the thermal and rheological state of the interior of the planetary embryo plays an important role for the mode of core formation, which has not been considered in detail in previous models.

[3] Recent results indicate that in addition to the above mentioned diapir formation mechanism at the base of the magma ocean or a local magma pond, which was modeled numerically by *Ziethe and Spohn* [2007], *Golabek et al.* [2008], *Samuel and Tackley* [2008], and *Ricard et al.* [2009], ongoing accretion of iron cores of larger predifferentiated impactors [*Taylor and Norman*, 1990] could be possible. These would have plunged intact through the magma ocean [*Dahl*, 2005; *Stevenson*, 2008] into the central region. Therefore, the differentiation process is likely to be more

dynamic than previously thought, with many mechanisms operating together.

[4] In our simplified model we assume Mars-sized planetary embryos and Earth-sized protoplanets, and apply as an initial condition a large group of randomly sized and randomly distributed iron diapirs inside the accreting planetary body. These can be thought to form from intact impactor cores or at the bottom of limited magma ponds created by impacts. We present models in which more realistic temperature-, pressure- and strain rate–dependent rheologies and effects such as shear heating and Peierls plastic deformation [*Kameyama et al.*, 1999] are considered. Depending on the applied Peierls stress, the friction angle, the activation volume and the temperature we identify several distinct core formation mechanisms, which will be presented in section 5. In section 6 we derive scaling laws identifying under which conditions plastic yielding and/or shear heating effects are important. It is demonstrated that shear heating induced thermal runaway related to the sinking of diapirs helps to cause yielding of silicate material and fosters core formation on short time scales.

2. Governing Equations and Numerical Methods

[5] We describe here the assumed conservation equations and their numerical implementation in the code employed for the main study (I2MART) and the code employed for verification of the

derived scaling laws (see section 5) (MILAMIN_ VEP), including the numerical techniques employed in these codes.

2.1. Conservation Equations

[6] We assume the extended Boussinesq equations in two-dimensional (2-D) geometry. The conservation of mass is approximated by the continuity equation.

$$\frac{D \ln \rho(T,P,c,t)}{Dt} + \frac{\partial v_x}{\partial x} + \frac{\partial v_z}{\partial z} = 0, \tag{1}$$

where D/Dt represents the substantive time derivative, the density $\rho(T,P,c,T)$ depends explicitly on temperature T, pressure P, composition c and time t. v_x and v_z are the x and z components of the velocity vector.

[7] The density varies with P-T conditions according to the relation:

$$\rho(P,T) = \rho[1 - \alpha(T - T_0)] \cdot [1 + \beta(P - P_0)], \tag{2}$$

where ρ is the density of the distinct material at T_0 = 298 K and $P_0 = 10^5$ Pa, α is the thermal expansion coefficient and β is the compressibility coefficient.

[8] The 2-D Stokes equations for creeping flow take the form:

$$\frac{\partial \sigma_{xx}}{\partial x} + \frac{\partial \sigma_{xz}}{\partial z} - \frac{\partial P}{\partial x} = -g_x(x,z,t)\rho(T,P,c) \tag{3}$$

$$\frac{\partial \sigma_{zz}}{\partial z} + \frac{\partial \sigma_{xz}}{\partial x} - \frac{\partial P}{\partial z} = -g_z(x,z,t)\rho(T,P,c), \tag{4}$$

where σ_{ij} represents the components of the deviatoric stress tensor. $g_x(x,z,t)$ and $g_z(x,z,t)$ are the x and z components of the local gravitational acceleration vector. It is worth noting that P is the total pressure, which includes both dynamic and lithostatic components.

[9] We have adopted a Lagrangian frame in which the heat conservation equation takes the following form [Gerya and Yuen, 2003]:

$$\rho(P,T,c,t)c_p\left(\frac{DT}{Dt}\right) = -\frac{\partial q_x}{\partial x} - \frac{\partial q_z}{\partial z} + H_S + H_a + H_r, \tag{5}$$

where c_p denotes isobaric heat capacity, and the heat flux q is defined as

$$q_x = -k\frac{\partial T}{\partial x} \text{ and } q_z = -k\frac{\partial T}{\partial z}, \tag{6}$$

where k is the thermal conductivity.

[10] Shear heating H_s is given by:

$$H_S = \sigma_{xx}\dot{\varepsilon}_{xx} + \sigma_{zz}\dot{\varepsilon}_{zz} + 2\sigma_{xz}\dot{\varepsilon}_{xz} \tag{7}$$

using

$$\dot{\varepsilon}_{ij} = \frac{1}{2}\left(\frac{\partial v_i}{\partial x_j} + \frac{\partial v_j}{\partial x_i}\right), \tag{8}$$

where $\dot{\varepsilon}_{ij}$ is the strain rate.

[11] H_a is the rate of adiabatic temperature increase given by:

$$H_a = T\alpha\left(v_x\frac{\partial P}{\partial x} + v_z\frac{\partial P}{\partial z}\right) \tag{9}$$

Finally H_r is the radioactive heating rate.

[12] We emphasize the presence of the shear heat production term H_s in the temperature equation because it is likely to have a significant [e.g., Gerya and Yuen, 2007], effect on the core formation process, but it has been ignored in many previous core formation studies with the exception of Samuel and Tackley [2008] and Ricard et al. [2009].

[13] We employ a viscous constitutive relationship between stress and strain rate with $\eta(T,P,\dot{\varepsilon},c)$ representing the effective viscosity, which depends on temperature, pressure, strain rate and composition:

$$\sigma_{ij} = 2\eta(T,P,\dot{\varepsilon},c)\dot{\varepsilon}_{ij}. \tag{10}$$

We use a silicate viscosity $\eta_{creep}(T,P,\dot{\varepsilon})$ which depends on temperature, pressure and strain rate defined in terms of deformation invariants [Ranalli, 1995] as:

$$\eta_{creep}(T,P,\dot{\varepsilon}) = (\dot{\varepsilon}_{II})^{(1-n)/n}(A)\exp\left(\frac{E_a + V_aP}{nRT}\right) \tag{11}$$

where $\underline{e}_{II} = \sqrt{\frac{1}{2}\underline{e}_{ij}\underline{e}_{ij}}$ is the second invariant of the strain rate tensor and A, E_a and n are the preexponential parameter, the activation energy and the power law coefficient, respectively. R is the gas constant and V_a is the activation volume. For silicates, this ductile rheology is combined with a brittle rheology to yield an effective viscoplastic rheology. For this purpose the Mohr-Coulomb [e.g., Ranalli, 1995] and Peierls [e.g., Kameyama et al., 1999] yield criteria are simultaneously implemented by limiting the creep viscosity as follows:

$$\eta_{creep}(P,\dot{\varepsilon}) \leq \frac{\sin(i)P + \chi}{2\dot{\varepsilon}_{II}} \tag{12a}$$

and

$$\eta_{creep}(\dot{\varepsilon}) \leq \frac{\sigma_P}{2\dot{\varepsilon}_{II}} \tag{12b}$$

Table 1. Physical Parameters and Their Values as Used for the Main Models and the Scaling Law Models

Parameter	Parameter Description	Value
R_P	radius of planetary body, m	$(3.5-6.0)\cdot10^6$
R_{Fe}	radius iron diapirs, m	$(0.5-2.0)\cdot10^5$
G	gravitational constant, $m^3/(kg\ s^2)$	$6.674\cdot10^{-11}$
κ	thermal diffusivity, m^2/s	$1\cdot10^{-6}$
c_P	specific heat capacity, $J/(kg\ K)$	$1.0\cdot10^3$
V_a	activation volume, m^3/mol	$0-8\cdot10^{-6}$
ρ_{Si}	density uncompressed silicates, kg/m^3	4000
ρ_{Fe}	density uncompressed iron, kg/m^3	8000
ρ_{SA}	density sticky air, kg/m^3	0
ρ_{SM}	density stabilizing material, kg/m^3	0
σ_P	Peierls stress (main model), Pa	$2.9\cdot10^9-10^{10}$
σ_P	Peierls stress (simplified model), Pa	$2.9\cdot10^9$
n_D	power law coefficient for dry olivine rheology	3.5
n_W	power law coefficient for wet olivine rheology	4.0
$sin(i)$	sine of friction angle (main model)	$0.01-0.6$
$sin(i)$	sine of friction angle (simplified model)	0.0
H_r	radioactive heating, W/kg	$3.05\cdot10^{-9}$
η_{Fe}	iron viscosity, Pa s	10^{19}
η_{Si}	solid silicate viscosity, Pa s	$10^{19}-10^{25}$
η_{SA}	sticky air viscosity, Pa s	10^{19}
η_{SM}	stabilizing material viscosity, Pa s	10^{25}
γ	e-fold length of viscosity, 1/K	0.10
E_{a-D}	activation energy for dry olivine rheology, J/mol	$5.32\cdot10^5$
E_{a-W}	activation energy for wet olivine rheology, J/mol	$4.70\cdot10^5$
A_{D-Si}	preexponential parameter for dry silicate material, Pa $s^{(1/n)}$	$3.98\cdot10^{16}$
A_{W-Si}	preexponential parameter for wet silicate material, Pa $s^{(1/n)}$	$5.10\cdot10^{20}$
R	universal gas constant, $J/(K\ mol)$	8.3145
α	thermal expansion coefficient, 1/K	$1\cdot10^{-5}$
β	compressibility coefficient, 1/Pa	$3\cdot10^{-12}$
μ	elastic shear modulus, Pa (MILAMIN_VEP only)	$5\cdot10^{100}$
h	heat retention factor	0.1
T_a	ambient temperature at accretion, K	273

where χ is the cohesion (residual strength at $P = 0$ Pa), i is the effective angle of internal friction and σ_P is the Peierls stress limit. Equation (12b) is a simple approximation of the usual Peierls law, with a simplified Peierls stress σ_P that is assumed to be independent of temperature and pressure. Plasticity is thus given here by the combination of Mohr-Coulomb (pressure-dependent part) and von Mises (Peierls part) criteria, from which the weakest stress limit is chosen locally. For numerical reasons, viscosity is cut off at lower and upper limits of 10^{19} and 10^{25} Pa s for silicates, whereas the iron viscosity is kept constant at 10^{19} Pa s. A similar value for the maximum silicate viscosity was suggested by *Karato and Murthy* [1997] as $10^{26\pm2}$ Pa s. One should note that the iron viscosity is, for numerical reasons, many orders of magnitude higher than its physical value, which is expected to range from 10^{-2} Pa s (in the liquid state) [*Rubie et al.*, 2007] up to 10^{12} Pa s in the solid state under high temperature and pressure conditions [*Yunker and Van Orman*, 2007]. The Peierls stress limit σ_P employed for the olivine rheology [*Ranalli*, 1995] (see also Table 1) ranged from $2.9 \cdot 10^9$ Pa to a maximum of 10^{10} Pa due to Frenkel's limit [*Frenkel*, 1926; *Scholz*, 2002].

2.2. Numerical Implementation in I2MART

[14] We have considered two-dimensional (2-D) creeping flow using the extended Boussinesq approximation, as discussed in section 2.1, in which both thermal and chemical buoyancy forces are included. We performed 2-D cylindrical simulations using the code I2MART by applying the methodology named "spherical-Cartesian" [see also *Gerya and Yuen*, 2007]. The methodology combines finite differences on a fully staggered rectangular Eulerian grid with a Lagrangian marker-in-cell technique for solving the momentum, continuity and temperature equations, and in order to model a cylindrical body on this Cartesian grid, it additionally calculates self-consistently the gravitational field for a self-gravitating accreting planetary body by solving the Poisson equation for gravitational potential (for details see *Gerya and Yuen* [2003, 2007] and *Lin et al.* [2009]). Hence gravity varies self-consistently with depth inside the planetary body. The method is most similar to the approach suggested by *Honda et al.* [1993] and also shares similarities with the methods presented by *Evonuk and Glatzmaier* [2006] and *Kotelkin and Lobkovsky* [2007]. The code uses the Pardiso sparse matrix solver [*Schenk and Gärtner*, 2004, 2006; http://www.pardiso-project.org/], which drastically reduces the calculation time compared

to standard solvers and enables us to perform higher-resolution calculations, encompassing a whole accreting planetary body. The experiments are performed using Brutus cluster of ETH Zurich.

2.3. Numerical Implementation in MILAMIN_VEP

[15] The governing equations described above are solved for a Cartesian domain with constant gravity field using the finite element (FE) code MILA-MIN_VEP, which employs a velocity–pressure formulation for the mechanical equations [e.g., *Moresi et al.*, 2003], with triangular elements for velocity and discontinuous linear shape functions for pressure. The applied mesh generator is Triangle developed by *Shewchuk* [1996]. For more details on the code see also *Kaus et al.* [2008]. The code is employed in a Lagrangian manner, in which the elements are deformed at each time step. If the elements are too distorted, remeshing is applied. Tracers are employed to track material properties. Material properties are computed from tracers by computing the dominant phase at each integration point, after which the integration point values are averaged over the element. Using tracers in combination with a Lagrangian FEM framework has the advantage that only local tracer coordinates are required (inside an element), since global coordinates can be retrieved by multiplying with the element shape function.

3. Model Setup

[16] Here we describe the setup applied in both the main model, in which the whole planetary embryo or protoplanet is modeled (section 5), and the simplified models employed to derive scaling laws describing the physics behind the results (section 6).

3.1. Model Setup for the Main Models

[17] In the code I2MART particles are employed to mimic different materials in each region and track their movement. The grid is uniform, and the resolutions applied ranged from 141 by 141 to 1401 by 1401 nodal points. The dimensional size of the model box is 14000 by 14000 km. The boundary condition for the gravitational potential is defined on the circular surface located at a distance of 6900 km from the center of the numerical box. As radii for the accreting planetary bodies we apply 3500 km (approximately Mars-sized planetary embryo, in comparison: $R_{Mars} = 3.397 \cdot 10^6$ m [*Lodders and Fegley*, 1998]) and 6000 km (approximately Earth-sized protoplanet, in comparison: $R_{Earth} = 6.371 \cdot 10^6$ m [*Lodders and Fegley*, 1998]).

[18] Iron diapirs are distributed throughout the planetary body except the outer 500 km below the surface. With currently available numerical techniques it is not yet possible to simulate the accretion of iron-rich material by the growing planetary bodies. Therefore we apply a simplified random diapir distribution inside the planetary body using random diapir radii within the range 50 to 100 km. 420 diapirs are positioned randomly in a Mars-sized planetary embryo and 1305 iron diapirs are inserted randomly into an Earth-sized protoplanet. We use for both position and size of the diapirs a Gaussian-like random distribution. Overlapping of iron diapirs is allowed. The number of iron diapirs in the planetary bodies is limited by the iron/silicate ratio of 0.3. This distribution represents a scenario in which the average collision time is shorter than the differentiation time (R. Ziethe et al., A consistent model for the accretion and differentiation of terrestrial planets: implications from the combination of Monte Carlo models for planet formation and finite element models for core formation, manuscript in preparation, 2009). One should, however, keep in mind that the size distribution of planetesimals and planetary embryos after runaway growth is likely to be an inverse power law of the form $N(D) \sim D^{-p}$, where D stands for the diameter of a body, $N(D)$ gives the number of objects equal to or greater than diameter D and where the exponent p is approximately 2 [*Melosh*, 1990]. If this size distribution applies to the diapir size then we would expect a large number of smaller diapirs and a few diapirs significantly larger than those used in our model, formed as the result of giant impacts [*Tonks and Melosh*, 1992; *Dahl*, 2005; *Stevenson*, 2008]. It can be expected that the largest impactors will influence the sinking behavior significantly. However, resolving the small diapirs numerically would require significantly higher resolution, which exceeds our current capabilities. Analytical results by *Tonks and Melosh* [1992] and numerical models of individual giant diapirs by *Ricard et al.* [2009] indicate that such a system might tend to runaway differentiation processes. A further numerical study examining the effect of giant impactor cores on the mode of core formation is currently under way [*Moll et al.*, 2009]. The presence of an already existing small iron core [*Yoshino et al.*, 2004; *Greenwood et al.*, 2005; *Terasaki et al.*, 2008; *Day et al.*, 2009] in an accreting planetary body

(a)

(b)
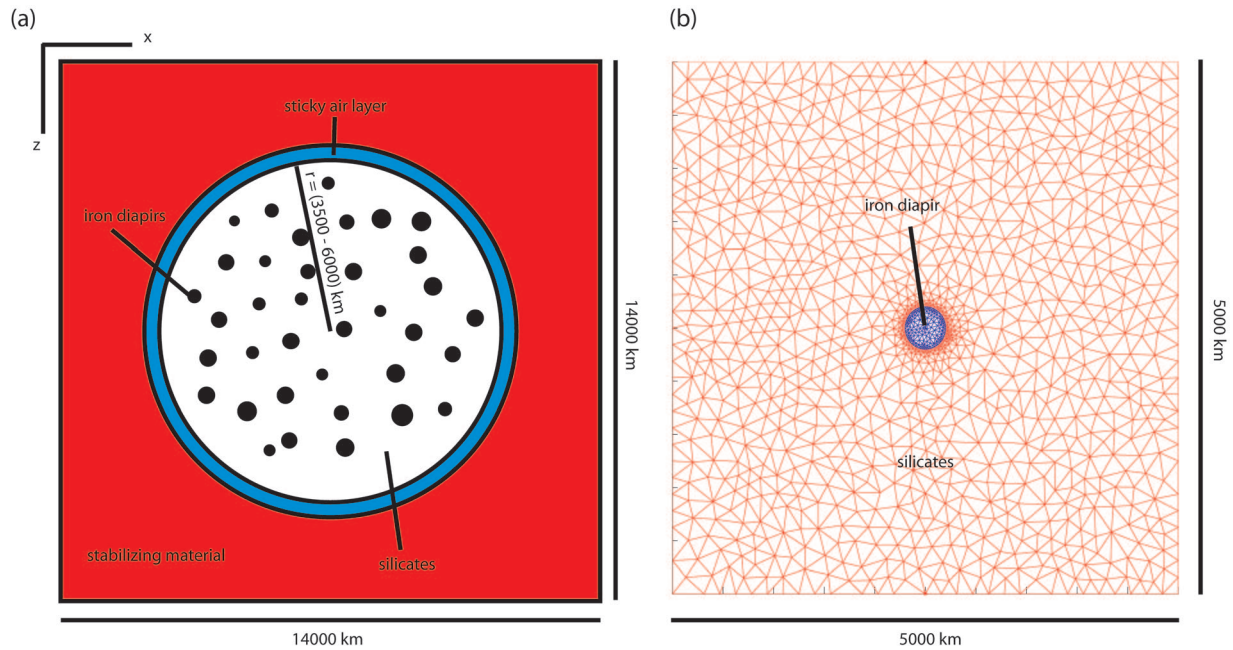
Figure 2. (a) Sketch of the applied initial setup including the accreting planetary body and its iron/silicate mixture, the sticky air layer, and the stabilizing material. (b) Typical example of the unstructured grid as applied in simplified calculations employed for the scaling analysis.

was neglected in all our models as test cases showed that is has only a second-order effect.

[19] In the used model, the accreting planetary body in the center of the numerical box is surrounded by a low-viscosity ($\eta_{SA} = 10^{19}$ Pa s), massless fluid ("sticky air"), whose upper limit is given by the position of the boundary condition for the gravitational potential. The thickness of the sticky air layer therefore ranges from 900 km for Earth-sized protoplanets to 3400 km for Mars-sized planetary embryos (see Figure 2a). We use this medium to mimic a free surface [see also *Schmeling et al.*, 2008]. The rest of the numerical box outside the sticky air layer is filled with a constant high-viscosity massless medium ($\eta_{SM} = 10^{25}$ Pa s) to ensure better numerical stability of the system and allow for larger time steps. Free-slip mechanical boundary conditions are applied at the sides of the model box.
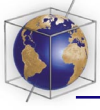
[20] The temperature of the sticky air layer and the stabilizing material is kept constant (273 K) during the experiment, providing the thermal boundary condition at the surface of the accreting body. The initial temperature is 273 K at the surface as we neglect a possible hot protoatmosphere surrounding the forming planetary body as suggested by, e.g., *Abe* [1997, and references therein], which could sustain a surface magma ocean.

[21] We use two end-member cases for the temperature profile: For the first case we neglect accretionary heating and take only radiogenic heating into account. The temperature rises linearly to more than 1300 K inside a Mars-sized planetary embryo (Figure 3a, black curve) and to 1800 K in the center of an accreting Earth-sized protoplanet (see Figure 3b, black curve). These initial profiles were chosen to mimic to zeroth order the effect of early short-lived radioactive heating inside the accreting planetary bodies. For the second case we neglect radioactive heating, but accretionary heating is taken into account. We use for the construction of this temperature profile the formula suggested by *Schubert et al.* [1986] and *Breuer and Moore* [2007], in which the temperature $T(r)$ at the radius r is given by:

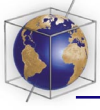$$T(r) = T_a + \frac{hGM(r)}{c_P r} \cdot \left[1 + \frac{rv^2}{2GM(r)} \right], \qquad (13)$$

where T_a is the ambient temperature during accretion, h is the fraction of the impact heating retained in the accreting body, G is the gravitational constant, $M(r)$ is the mass of the planetary body within radius r, and v is the approach velocity of impactors. The approach velocity can be given to a good approximation as the escape velocity of a planetary body of radius r, given as $v = \sqrt{\frac{2GM(r)}{r}}$ [e.g., *Agnor et al.*, 1999].
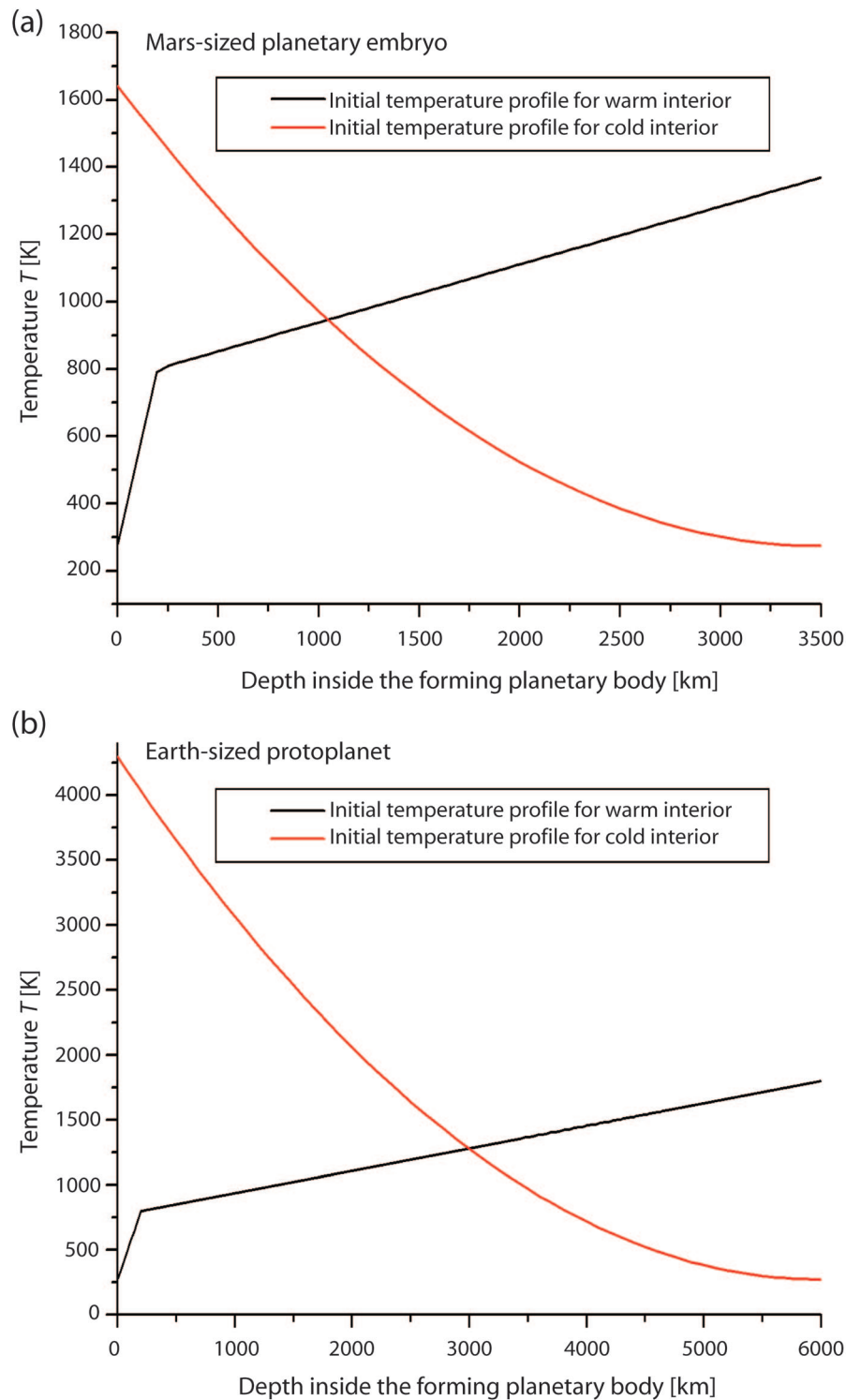
Figure 3. Initial temperature profiles for (a) Mars-sized planetary embryos and (b) Earth-sized protoplanets applied in the numerical models. In both Figures 3a and 3b red curves represent the temperature profiles calculated using equation (13), which take accretionary heating into account but, however, neglect short-lived radioactive heating and yield a cold planetary interior, whereas the black curves simulate a possible temperature profile when the decay of short-lived radioactive isotopes is taken into account and impact heating is neglected.

[22] We apply a conservative value of 0.1 for the retained impact heat h and for the ambient temperature T_a a value of 273 K. The resulting temperature profile is shown in Figures 3a and 3b (red curves). One should keep in mind that the relation given in equation (13) only holds until the temperature in the outer portion of the body reaches silicate melting, therefore it is valid for a Mars-sized planetary embryo (see introduction), but is unrealistic for an Earth-sized protoplanet as it neglects the onset of vigorous convection [*Melosh*, 1990].

[23] For both end-member models we consider additional radioactive heating with H_r = 3.05 · 10^{-9} W/kg, which is the heating rate expected at 4.3 Ma after CAI formation. This value was obtained by taking all important short-lived (^{26}Al, ^{60}Fe) and long-lived radioactive isotopes (^{40}K, ^{235}U, ^{238}U, ^{232}Th) and their initial concentrations in the early solar system into account. The assumed starting time lies between the extreme time scales for the formation of Mars-sized planetary embryos compiled by *Chambers* [2004]. Data for the radiogenic heating were taken from *Barr and Canup* [2008, Table 3]. The radioactive heating is kept constant. Recent results by *Ziethe and Spohn* [2007] show that consideration of temperature-dependent rheology may increase the sinking velocity of iron diapirs considerably in comparison to the Stokes sinking velocity in an isoviscous medium [see also *Weinberg and Podladchikov*, 1994]. Therefore we use a temperature-dependent viscoplastic rheology. Additionally we take shear heating and the adiabatic temperature gradient into account.

[24] Since our knowledge about planetary accretion is limited, there is an enormous parameter space to explore for the given model setup. In this initial study we focus on the influence of rheology. Although different minerals exist at high pressure, for simplicity, and because the rheology of accreting terrestrial bodies is highly uncertain, we approximate silicate rheology at all pressures using a single preexponential parameter A, activation energy E_a, and activation volume V_a and power law exponent n. We varied the following parameters: The activation volume V_a is chosen to be between 0.0 and 8 · 10^{-6} m³/mol. These values are representative of wet and dry olivine rheology [e.g., *Mei and Kohlstedt*, 2000a, 2000b]. The sines of the friction angle sin i were varied between 0.01 (i = 0.6°) and 0.6 (i = 36.9°).

[25] The Peierls stress is proportional to the shear modulus μ. The shear modulus of olivine is $\mu \sim 8$ · 10^{10} Pa [*Poirier*, 2000]. Following *Scholz* [2002] the maximum yield stress is around 1/10 of the shear modulus, so realistic Peierls stress limits inside olivine rheology dominated planetary bodies explored in this study should be below or close to 10^{10} Pa. The Peierls stress σ_P (see equations (12a) and (12b)) of 2.9 · 10^9 Pa as suggested for wet [*Katayama and Karato*, 2008] and of 9.1 · 10^9 Pa for dry olivine rheology [*Evans and Goetze*, 1979] fit this criterion and are used in our models. Additional models were performed with Peierls stresses of 10^{10} Pa.

[26] To ensure the comparability of models with different rheological parameters we do not vary the initial temperature profile, but assume the two end-member cases discussed above, scaled to either Mars-sized planetary embryos or Earth-sized protoplanets. Most experiments have the "radiogenic heating" temperature profile with a warm central region. We perform additional experiments using the "accretional heating" temperature profile containing a cold central region for V_a = 0 and 8 · 10^{-6} m³/mol and sin i = 0.6 for both wet and dry rheology on both Mars-sized planetary embryos and Earth-sized protoplanets. Further parameters are given in Table 1.

3.2. Model Setup for the Scaling Law Model

[27] To better understand the underlying physics of the different behaviors of the diapirs observed in the main model, we explore a simplified model, where only one iron diapir is sinking through the viscoplastic medium. The resting diapir is initially positioned in the center of a square box of 5000 km side length to avoid influence from the boundaries (see Figure 2b). Gravity acts only in the z direction. Free slip boundary conditions are applied. Thermal boundary conditions are isothermal for the top and bottom and zero flux on the sides. The diapir radius is varied between 50 and 600 km and an uniform gravitational acceleration is applied throughout the whole box. Therefore the diapir reaches its terminal velocity on a short time scale.

[28] The same rheological parameters for the iron diapir and the silicate material are assumed as in the calculations performed with I2MART and are given in Table 1, except that here we use sin i = 0 and set the cohesion equal to the Peierls stress as the friction angle has an influence on the plastic behavior only at low pressures [see *Scholz*, 2002]

Table 2. Physical Parameters and Their Values as Used for the Resolution Test for Both Codes I2MART and MILAMIN_VEP

Parameter	Parameter Description	Value
g	gravity acceleration, m/s^2	10
ρ_{SiR}	silicate density, kg/m^3	4000
ρ_C	cylinder density, kg/m^3	8000
η_{SiR}	silicate viscosity, Pa s	10^{21}
η_C	cylinder viscosity, Pa s	10^{25}
r_C	radius of the cylinder, m	$2.5 \cdot 10^4 - 2.0 \cdot 10^5$

and no radioactive heating is taken into account. As results by *Samuel and Tackley* [2008] indicate that shear heating is mostly important within a narrow region surrounding the diapir, an unstructured mesh is employed in these simulations to resolve this effect properly (see again Figure 2b). To effectively switch off elastic effects a very high shear modulus μ is used. For the physical parameters employed see also Table 1.

4. Resolution Test

[29] First we perform a resolution study for our model to test what grid resolution is sufficient to capture the physics of a single diapir sinking. In these tests we employ a numerical box of size 4000 by 4000 km including one sinking cylindrical diapir in the center of the box with radius ranging from 25 to 200 km (similar to the setup shown in Figure 2b and the setup employed by *Popov and Sobolev* [2008]). We assume constant, distinct densities and viscosities for both media. Gravitational acceleration g is kept constant throughout the box. For other parameters employed in the resolution test, see Table 2.

[30] Comparison of 2-D models with the classical Stokes formula is problematic because of the so-called Stokes paradox. However, under special conditions, an appropriate analytical description for the sinking of 2-D cylinders can be obtained as has been done by *Slezkin* [1955] under the assumptions of a stiff cylinder in a box with no slip boundary conditions. We compare the numerical results with this analytical solution.

[31] The analytical sinking velocity is given as

$$v_C = \frac{1}{4}\left(\ln k - \frac{k^2 - 1}{k^2 + 1} \right) \cdot \left(\frac{\Delta \rho g r_C^2}{\eta_{SiR}} \right), \quad (14)$$

where v_C is the sinking velocity of the cylinder, $\Delta \rho$ is the density contrast between both media, r_C is

the radius of the cylinder and η_{SiR} is the viscosity of the surrounding medium. k is defined as $k = \frac{w}{r_C}$, where w is the distance between the cylinder and walls of the box.

[32] As can be seen in Figure 4a, results indicate that both codes reproduce the sinking velocity within a few percent. The systematic shift to higher velocities observed for both codes when modeling a large cylinder is due to the proximity of the cylinder to the model boundaries.

[33] We observe that in the diapir radius range of 50 to 100 km employed in the main model, velocity errors are between 1 and 6.5% when applying grid sizes of 16 to 32 km. Therefore a grid resolution of 501x501 nodal points ($\Delta x = 28$ km) is sufficient to reproduce the general dynamics of the differentiation process.

[34] To confirm this, we perform an additional resolution test with one of the main models (the same depicted in Figure 7) by using resolutions between 501 and 1401 nodal points. We plot the ratio between iron and silicates in the central region of the differentiating body over time (see Figure 4b). As can be seen, a resolution of 501x501 nodal points is sufficient to describe the process (see also Appendix A).
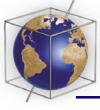
5. Results: Core Formation Modes for Different Initial Temperature Profiles

[35] In this section we will describe the different regimes of core formation observed during the parameter studies using a viscoplastic rheology. We vary the following parameters: activation volume V_a, friction angle i, Peierls stress σ_P and the radius of the accreting planetary body R_P. At the beginning of each section we give a short description of the governing physics for each particular core formation mode and a short overview of the conditions under which this mode develops as well as a schematic distribution of the different core formation modes observed in the explored parameter range given in Figures 5a and 5b. Afterward the transient evolution of a representative model for the particular mode is described.

5.1. Core Formation Modes for a Warm Interior

5.1.1. Collective Diapirism Mode

[36] This mode is characterized by plastic yielding and shear heating instabilities throughout the entire
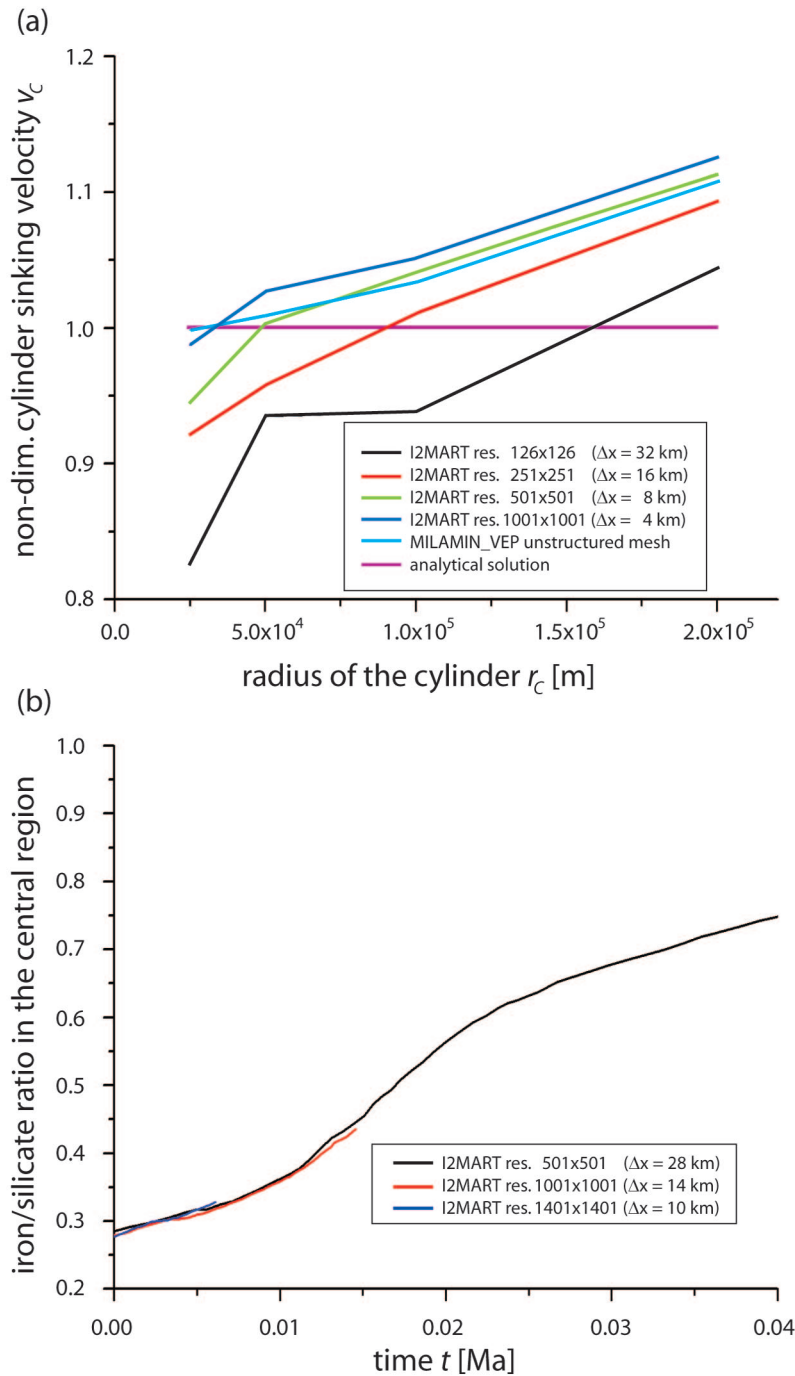
Figure 4. (a) Resolution test, using both I2MART and MILAMIN_VEP, for a cylindrical body with a 4000 kg/m³ higher density than employed for the background material. The cylindrical body has a viscosity 10⁴ times higher than the background viscosity and is situated in the center of a square box. Boundary condition at all box sides is no slip. The ordinate shows the sinking velocity of the cylinder, scaled by $\frac{1}{4}\left(\ln k - \frac{k^2-1}{k^2+1}\right)\left(\frac{\Delta\rho g r_C^2}{\eta_{SiR}}\right)$. (b) Resolution test applying I2MART on an Earth-sized protoplanet. Shown is the iron/silicate ratio in the central region of the body, which has a radius of 2350 km. It can be seen that the result obtained with 501 × 501 nodal points is in close agreement with model results for 1001 × 1001 and 1401 × 1401 grid points. In addition, the results show that the iron silicate separation in the central region is very efficient.
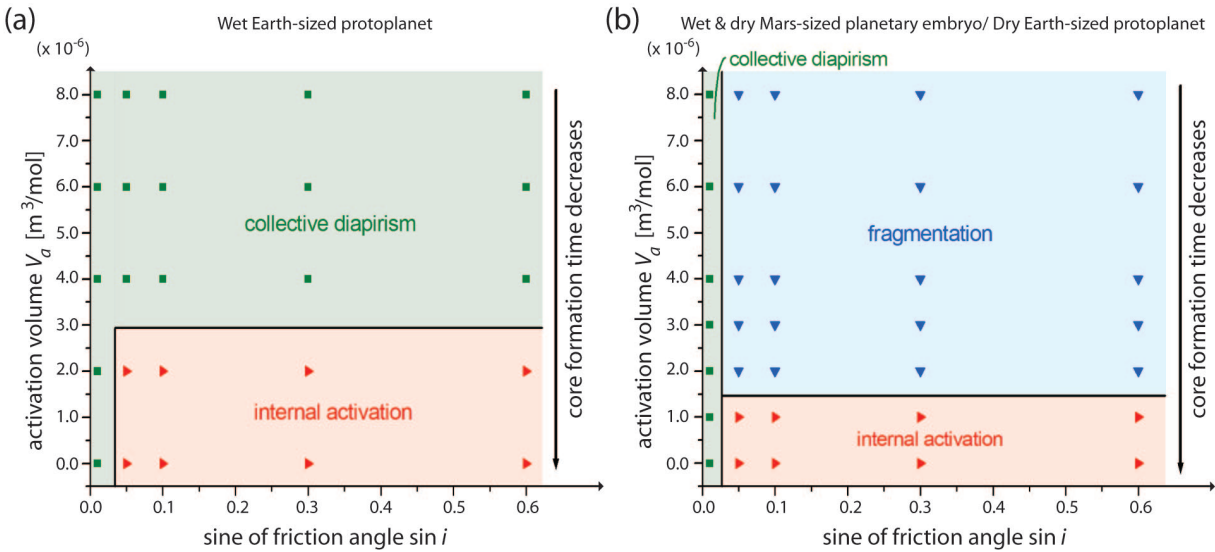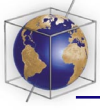
Figure 5. Schematic distribution of core formation modes in (a) an Earth-sized protoplanet with wet olivine rheology and (b) Mars-sized planetary embryos with wet and dry rheology and Earth-sized protoplanets with dry olivine rheology in the parameter space consisting of sine of the friction angle versus activation volume.

planetary body as the silicate viscosity of the entire body is weak (see Figure 6a). Core formation in this mode is largely finished within 0.1 Ma (see Figure 7).

[37] We observe the occurrence of collective diapirism (see Figures 5a and 5b) for the following physical parameters: (1) on Mars-sized planetary embryos with both wet ($\sigma_P = 2.9 \cdot 10^9$ Pa) or dry ($\sigma_P = 9.1 \cdot 10^9$ Pa) olivine rheologies for all activation volumes V_a, as long as sin i < 0.05; (2) on Earth-sized protoplanets with both wet and dry olivine rheology for all activation volumes V_a, as long as sin i < 0.05; and (3) on Earth-sized protoplanets for wet olivine rheologies for the whole explored parameter range of friction angles and activation volumes $V_a > 2 \cdot 10^{-6}$ m³/mol.

[38] For typical models dominated by the collective diapirism mode, plastic yielding of the silicates rather than ductile creep activates the iron diapir motion (see Figure 6a). This is possible as the pressure dependency of material strength (and its effective viscosity) is negligible in the plastic creep regime (either because of the low i in equation (12a) or because of no pressure dependence in equation (12b)) and the material is generally weak. The plastic yielding results in a drastic reduction of effective viscosity in the vicinity of iron diapirs, and shear heating instabilities develop. This results in a very short core formation time scale as the yield zones are present throughout the entire planetary body and the iron diapirs tend to sink collectively

instead as single isolated bodies. The formation of the collective groups can be understood as being a Rayleigh-Taylor like instability induced by slight differences in the mean density between the overlying and underlying iron/silicate mixture [*Sasaki and Abe*, 2007]. Numerical results by Y. Deubelbeiss et al. (Direct numerical simulation of two-phase flow: Effective rheology and flow patterns of particle suspensions, submitted to *Earth and Planetary Science Letters*, 2009) indicate that a wide spacing between the sinking spheres is needed for the transition into the classical single diapir sinking mode described in previous numerical models [e.g., *Ziethe and Spohn*, 2007; *Samuel and Tackley*, 2008; *Golabek et al.*, 2008].

[39] Results indicate that the release of potential energy due to the sinking of diapirs is concentrated in the narrow yield zones behind sinking diapirs and can provide effective pathways for subsequent diapirs. Similar phenomena have been observed in numerical experiments by *Ziethe and Spohn* [2007] and *Samuel and Tackley* [2008], as well as in laboratory experiments by *Olson and Weeraratne* [2008] (see Figure 7). Strong shearing of the iron material inside the channels and the formation of elongated iron structures is observed.

[40] Highly irregular distributed thermal upwellings form from the wakes left behind by the collectively sinking diapirs. Inside these regions, convection is vigorous as they are several thousand degrees hotter than the surrounding material. Yet,
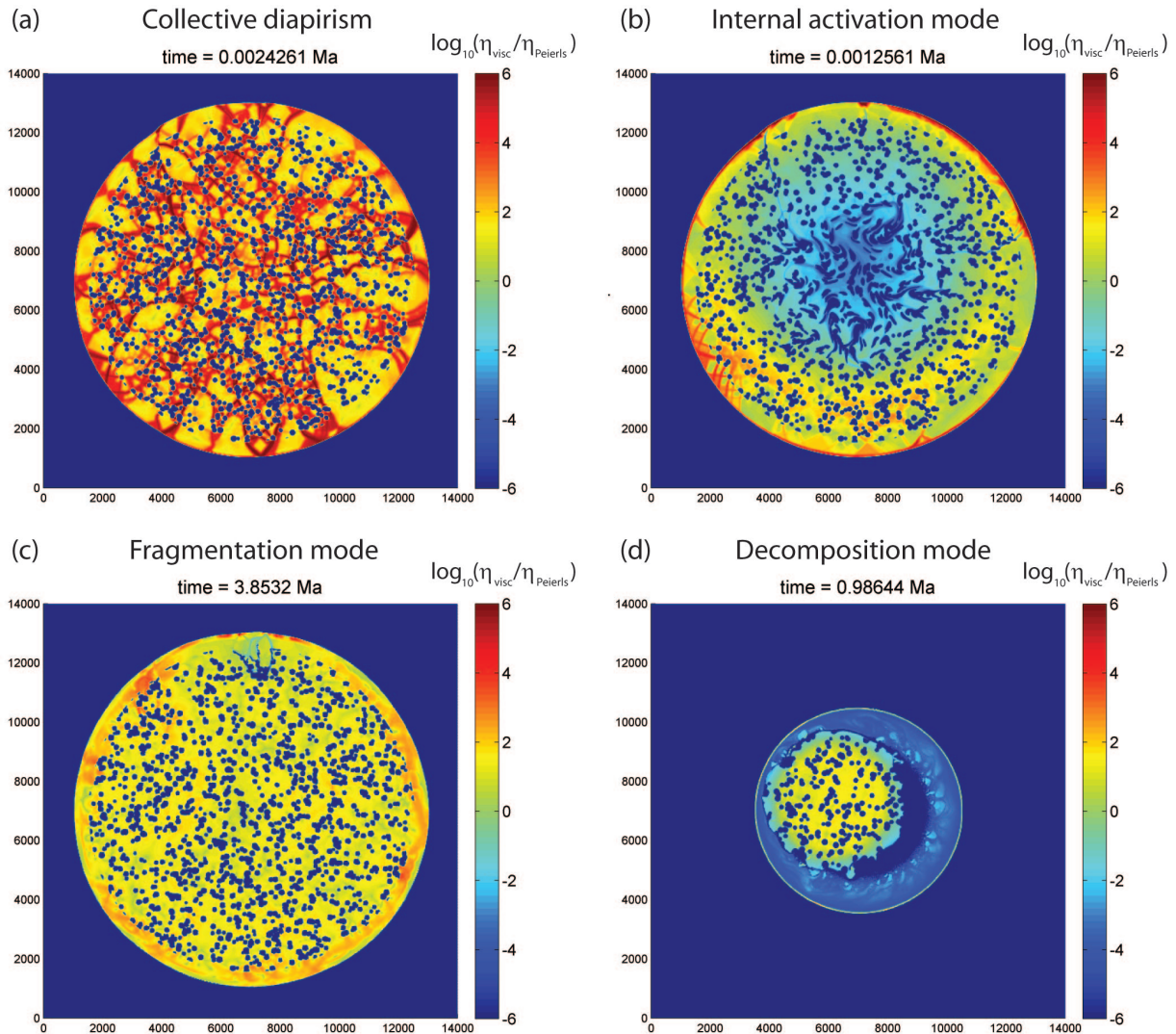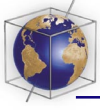
Figure 6. Shown on the marker level are which deformation mechanisms are active inside a planetary body. Values larger than 0 indicate that the plastic regime dominates, whereas negative values indicate the viscous regime. (a) It can be seen that the collective behavior is dominated by plastic deformation throughout the planetary body whose silicates consist of wet olivine material. (b) For the internal activation mode the central region is in the viscous regime and shows Rayleigh-Taylor instabilities, whereas the outer region stays stiff with both mechanisms equally important. (c) The deformation mechanisms active for the fragmentation mode are depicted. It can be seen that generally, both plasticity and shear heating are about equally important in this case; however, the activation of diapir groups is due to shear heating instabilities and not plasticity. (d) In the decomposition mode the outer shell behaves viscously and rapidly forms an iron ring, whereas the inner stiff region is equally controlled by both mechanisms.

vaporization does not limit the temperature rise deep inside the growing planetary body, because of the high pressure [*Tonks and Melosh*, 1993], although melting would influence the temperature if it were included in our model. The sinking of iron diapir groups inside these channels is nevertheless possible due to their strong negative buoyancy, whereas the sinking of single small-sized diapirs may be hindered in convective channels. The remaining iron material, which was initially situated in regions where the iron fraction was lower and

plastic yielding was not possible, making sinking very slow, is trapped in small fragments of silicate.

[41] The friction angle i seems to have a negligible effect on the general behavior, except when it has an extremely small value, since Peierls plastic strength (equation (12b)) is almost always overcome in this case. With decreasing activation volume the focusing of the channels becomes weaker and a generally hot mantle develops.
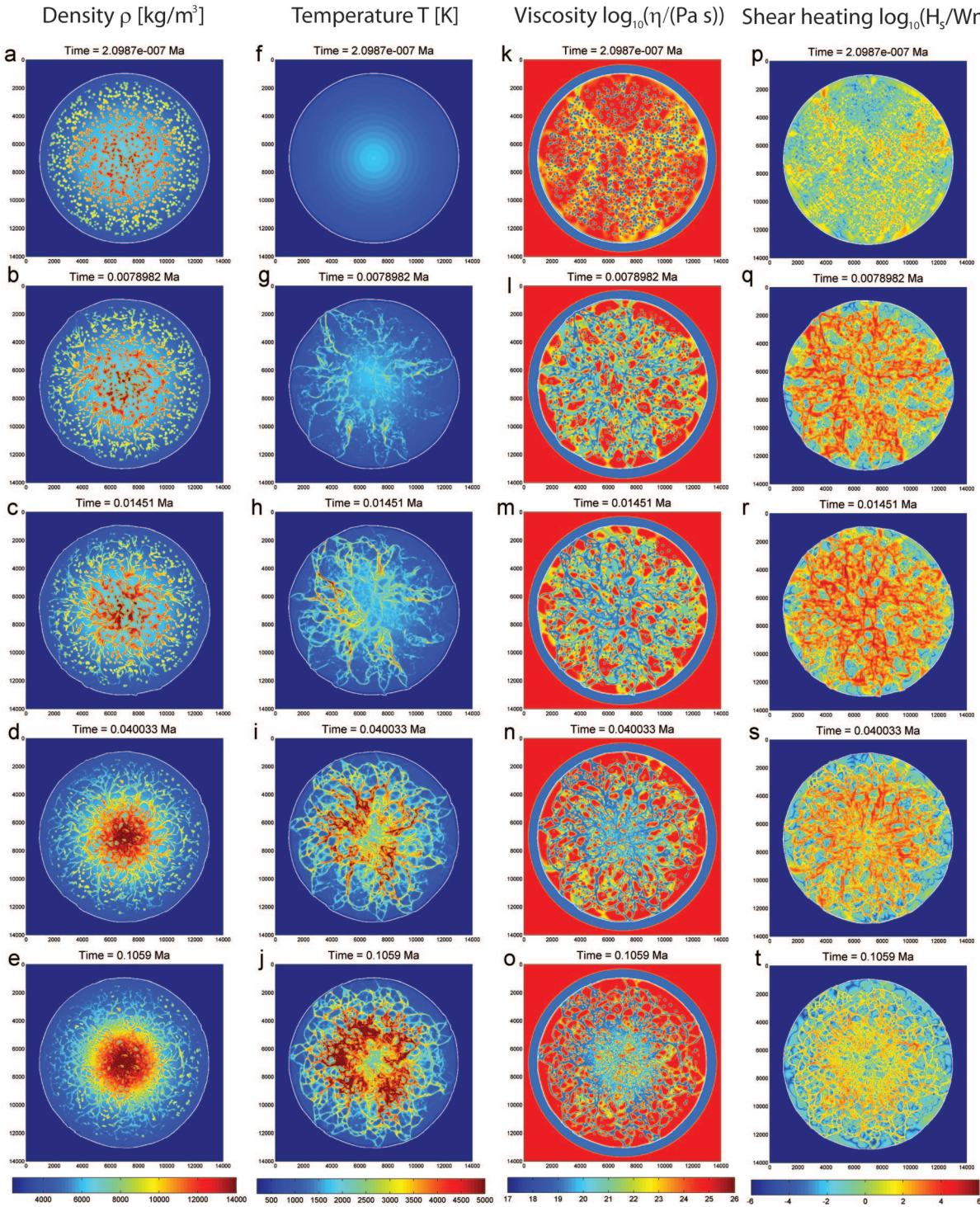
Figure 7. Shown are density, temperature, viscosity, and shear heating for different time steps for a typical example of the collective behavior regime in an Earth-sized protoplanet. The simulation shown employs the following parameters: $V_a = 8 \cdot 10^{-6}$ m³/mol, sin $i = 0.6$, and $\sigma_P = 2.9 \cdot 10^9$ Pa. (a–e) The density field. (f–j) The temperature field in Kelvins. (k–o) The logarithm of the viscosity. (p–t) The amount of shear heating released inside the planetary body applying a logarithmic scale. The white line shown in all plots is the 273 K isotherm and marks the current surface of the protoplanet. Animations S3–S6 in the auxiliary material show the collective diapirism mode.
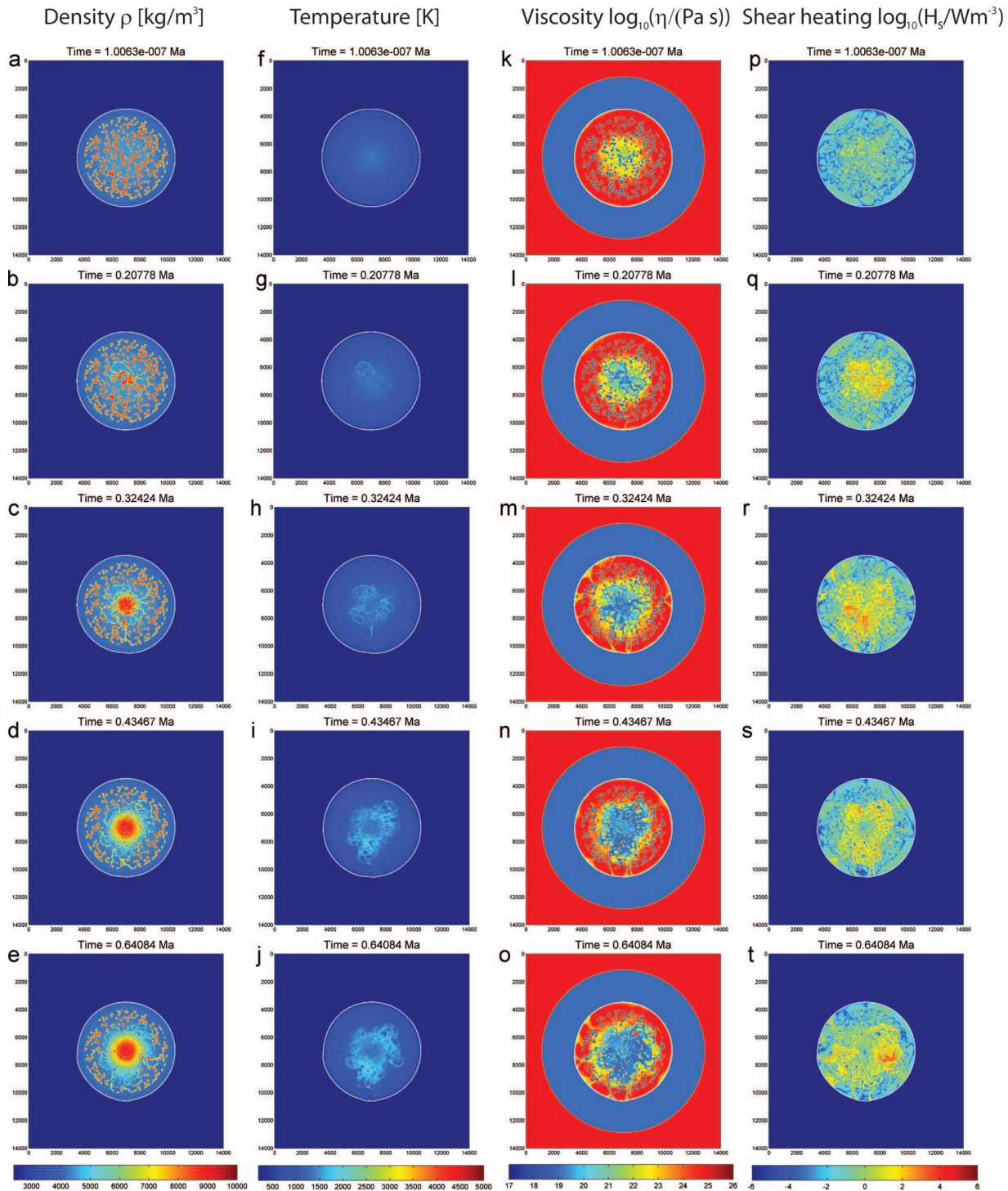
Figure 8. Same configuration as in Figure 7 but for a case applying $V_a = 2 \cdot 10^{-6}$ m³/mol, sin $i = 0.3$, and $\sigma_P = 9.1 \cdot 10^9$ Pa showing a typical example for the internal activation mechanism on a Mars-sized planetary embryo. Note that the scales are the same as in Figure 7 except that a lower visualization cutoff for density fields is used Animations S7−S10 in the auxiliary material show the internal activation mode.

5.1.2. Internal Activation Mode

[42] In this mode the rheology of the inner region of the accreting planetary body is weak and Rayleigh-Taylor instabilities develop, which lead to and are amplified by shear heating instabilities (see Figure 6b), whereas the outer regions are initially stiff. An iron core forms rapidly, however significant amounts of iron are trapped in the outer rigid shell (see Figure 8).

[43] The internal activation mode is illustrated in Figure 8 and is observed for the following models (see also Figure 5): (1) on Mars-sized with both wet ($\sigma_P = 2.9 \cdot 10^9$ Pa) and dry ($\sigma_P = 9.1 \cdot 10^9$ Pa) rheology and on Earth-sized bodies with dry olivine rheology in cases where the activation volumes are low ($V_a < 2 \cdot 10^{-6}$ m³/mol) and a friction angle sin $i > 0.01$ and (2) on Earth-sized bodies with wet olivine rheology for $V_a < 3 \cdot 10^{-6}$ m³/mol) and a friction angle sin $i > 0.01$.

[44] As the interior viscosity is weak (due to high T and low V_a), small iron diapir agglomerations or even single diapirs are able to sink in several very broad groups toward the center of the growing planetary body. The energy release on a short time scale heats the central region of the forming planetary body by an amount that is dependent on its radius by several hundred (Mars-sized planetary embryo) to several thousand (Earth-sized protoplanet) degrees and induces vigorous convection inside the inner region of the body (see Figure 8), thereby fostering rapid core segregation. The temperature differences can be explained by the difference in potential energy release, the amount of which is strongly controlled by the radius of the planetary body ($\sim R_P^5$) [see *Schubert et al.*, 1986]. An iron core forms on short time scales ($t < 1$ Ma) on both Mars- and Earth-sized bodies. Cooling of the body is only possible via conduction through a thick highly viscous lid. The material at the lower boundary of the stagnant lid is bottom heated and detaches as Rayleigh-Taylor instabilities of various wavelengths, which release additional energy into the inner regions of the body. The blocks decompose in the hot interior into silicates and iron. On Mars-sized planetary embryos the released energy is insufficient to induce thermal upwellings and the lid is slowly destroyed due to the above described mechanisms (see Figure 8). When the thickness of the upper shell is reduced to about half of its initial thickness, deviatoric stresses induced by the thermal upwellings exert a sufficient deviatoric stress on the lid to induce shear heating instabilities in the stagnant lid and penetrate to the surface of the body. However, on Earth-sized bodies convection is more vigorous and induce the shear heating instabilities in the lid immediately after core formation. In both cases this results in rapid fragmentation of the floating shell that is repeated in a similar manner all over the planetary body. Despite of the short time scale of the whole process, we may expect that in reality incoming giant impactors can break or weaken the lid and thus allow for more efficient cooling of the body, which would reduce the convective vigor inside the accreting planetary body.
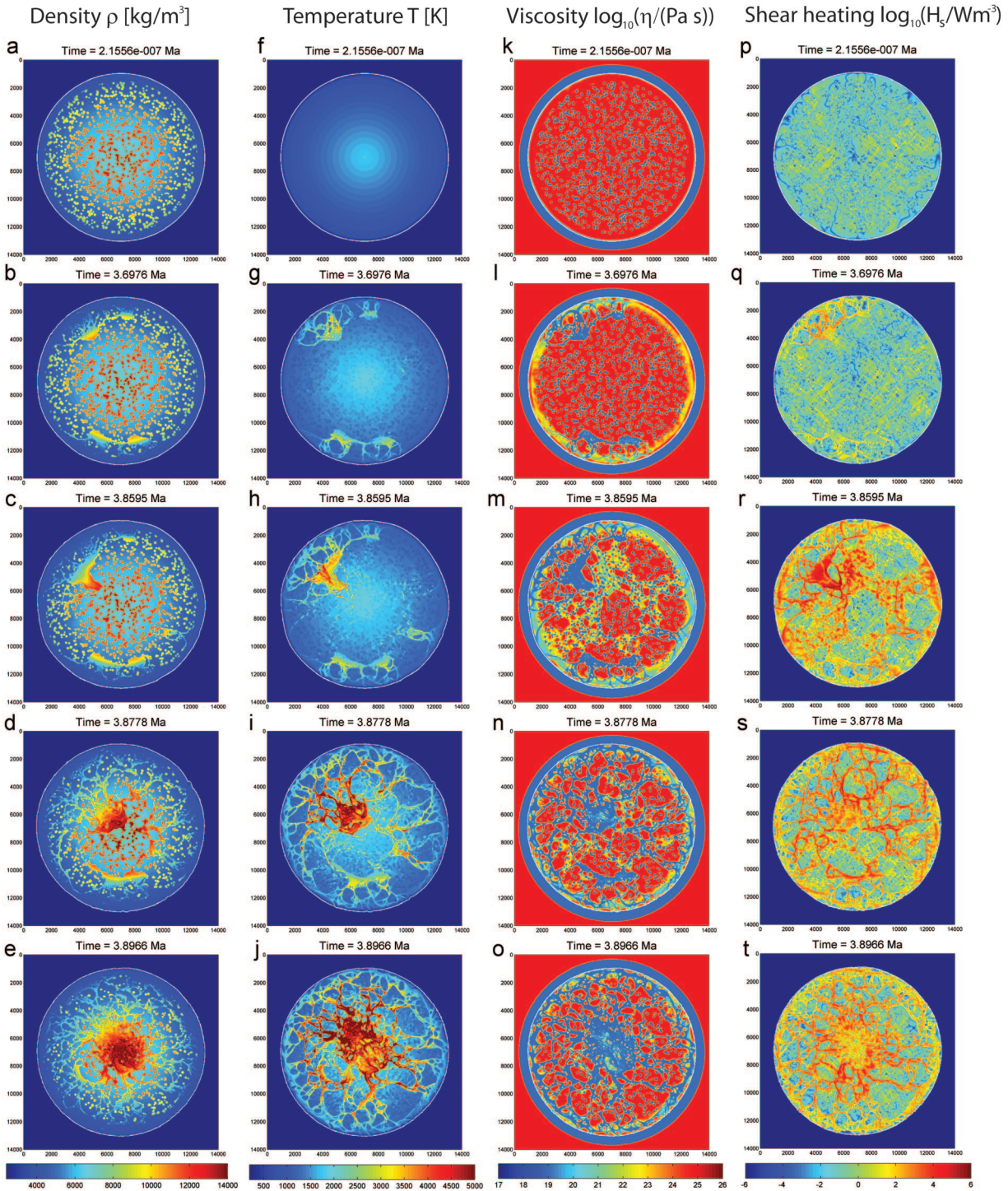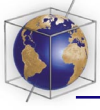
5.1.3. Fragmentation Mode

[45] In this mode the rheology of the whole planetary body is stiff until radioactive heating weakens the silicate material. Shear heating instabilities can then occur (see Figure 6c), which help to fragment first the outer shell and afterward the inner regions of the planetary body into distinct rigid blocks (see Figures 9 and 10).
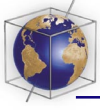
[46] The fragmentation mode is illustrated in Figures 9 and 10 and was observed in the following models (see also Figure 5b): (1) on Mars-sized planetary embryos with both wet ($\sigma_P = 2.9 \cdot 10^9$ Pa) and dry ($\sigma_P = 9.1 \cdot 10^9$ Pa) rheology and an activation volume ($V_a \geq 3 \cdot 10^{-6}$ m³/mol) with sin $i \geq 0.05$ and (2) on Earth-sized protoplanets with dry rheology employing an activation volume ($V_a \geq 2 \cdot 10^{-6}$ m³/mol) with sin $i \geq 0.05$.

[47] In this mode the whole planet is initially highly viscous (as V_a is large), radiogenic heating increases the temperature of the medium and fosters after several Ma the formation of the first shear heating instabilities in the upper regions of the planetary body (see Figure 6c). In regions where, due to the initial distribution, a larger fraction of iron is present, diapirs induce shear heating instabilities in the underlying material first as these groups generate a higher deviatoric stress. Iron diapirs propagate rapidly downward and coalesce into larger iron ponds. The temperature in the shear bands is higher than in the surrounding material, which assists in the transport of adjacent iron diapirs. With further warming of the body's interior, new shear heating instabilities progressively develop and the iron ponds sink deeper and grow larger in size until at a certain point their size is sufficiently large to penetrate to the center of the planetary body. During this process, the planetary body is "sliced" into numerous distinct "rockbergs" as suggested by *Stevenson* [1981], which are separated by weak shear bands.

Figure 9. Same configuration as in Figure 7 but showing a case with $V_a = 6 \cdot 10^{-6}$ m³/mol, sin $i = 0.3$, and $\sigma_P = 9.1 \cdot 10^9$ Pa, which depicts a typical example for the fragmentation mechanism observed for an Earth-sized protoplanet. The scales are the same as in Figure 7. Animations S11–S14 in the auxiliary material show the fragmentation mode on an Earth-sized protoplanet.
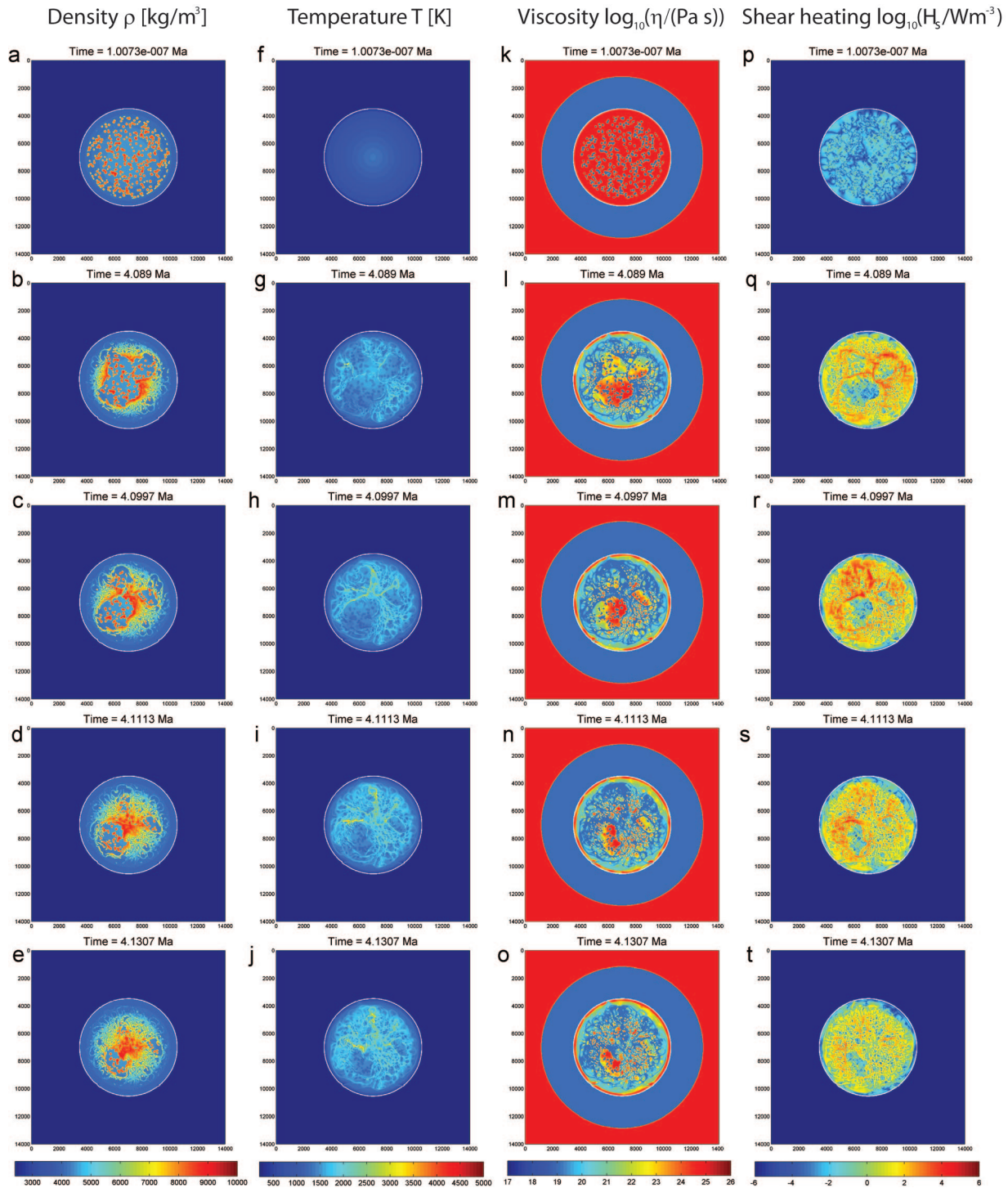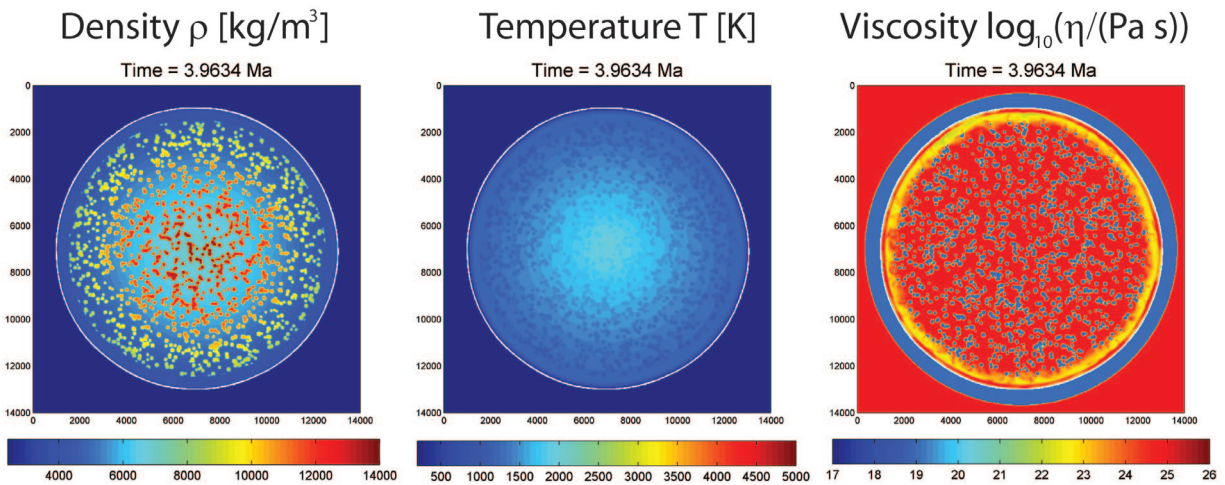
Figure 10. Same configuration as in Figure 7 but showing a case with $V_a = 8 \cdot 10^{-6}$ m³/mol, $\sin i = 0.6$, and $\sigma_P = 9.1 \cdot 10^9$ Pa, which depicts a typical example for the fragmentation mechanism observed here on a Mars-sized planetary embryo. Note that the scales are the same as in Figure 7 except that a lower visualization cutoff for density fields is used.

Figure 11. The same model setup is applied as for the case shown in Figure 9 except that no shear heating is taken into account. Shown are density, temperature, and viscosity for a time step comparable to the one shown in Figures 9e, 9j, and 9o. It is apparent that in this case the lack of shear heating leads to a drastically slower differentiation as no high-temperature bands, which could lead to fragmentation, can develop.

[48] The release of potential energy due to the sinking iron diapirs in the channels results in a positive feedback, which keeps the iron material in the shear bands at high temperatures. After the bulk of core formation is finished, remnant rockbergs can still contain iron material. They are fragmented by shear localization induced by the remaining iron diapirs they contain, when the temperature of the fragments rises sufficiently. On both Mars- and Earth-sized bodies, core formation is largely finished within ~4 Ma.

5.1.3.1. Very Stiff Silicate Viscosity

[49] We performed additional models applying a very stiff rheology at Frenkel's limit [*Frenkel*, 1926] with a Peierls stress of 10^{10} Pa. Results indicate that for such planetary bodies the fragmentation mode still prevails although the core formation time is increased because larger iron ponds must form before they are able to yield the underlying material.

5.1.3.2. Importance of Shear Heating for the Fragmentation Mode

[50] To estimate the influence of shear localization in this core formation mode, we performed one model for an Earth-sized protoplanet without taking shear heating into account, which shows a completely different behavior (see Figure 11): The lack of shear heating instabilities prohibits the development of clearly defined high-temperature bands. The iron diapirs sink very slowly as Stokes spheres through the highly viscous medium.
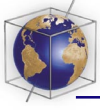
Thus, the core formation process is prolonged significantly. No fragmentation into distinct rockbergs takes place.

[51] These two additional tests, together with the results in section 5.2 indicate that only low silicate temperatures have the potential to yield an additional core formation mechanism, where the central region is moved out from the center of the planetary body as it was first suggested by *Elsasser* [1963].

5.2. Core Formation Modes for a Cold Interior: Decomposition Mode

[52] In comparison to the results in section 5.1, we apply here an inverted temperature profile with a cold planetary interior (see equation (13) and the red curves in Figures 3a and 3b). In most cases we observe the appearance of basically the same core formation modes as observed in section 5.1. The hot outer regions of the forming planetary bodies are dominated by the collective diapirism mode, whereas the cold central regions experience in most cases the fragmentation mode because of the high deviatoric stresses exerted by the forming iron ponds. Only under favorable conditions is a fourth core formation mode (mentioned in section 5.1.3) observed, and this is described below.

[53] In this mode the highly viscous inner region of the planetary body is moved out from the center of the body via only Stokes flow, as neither plastic yielding nor shear localization occur (see Figure 6d).
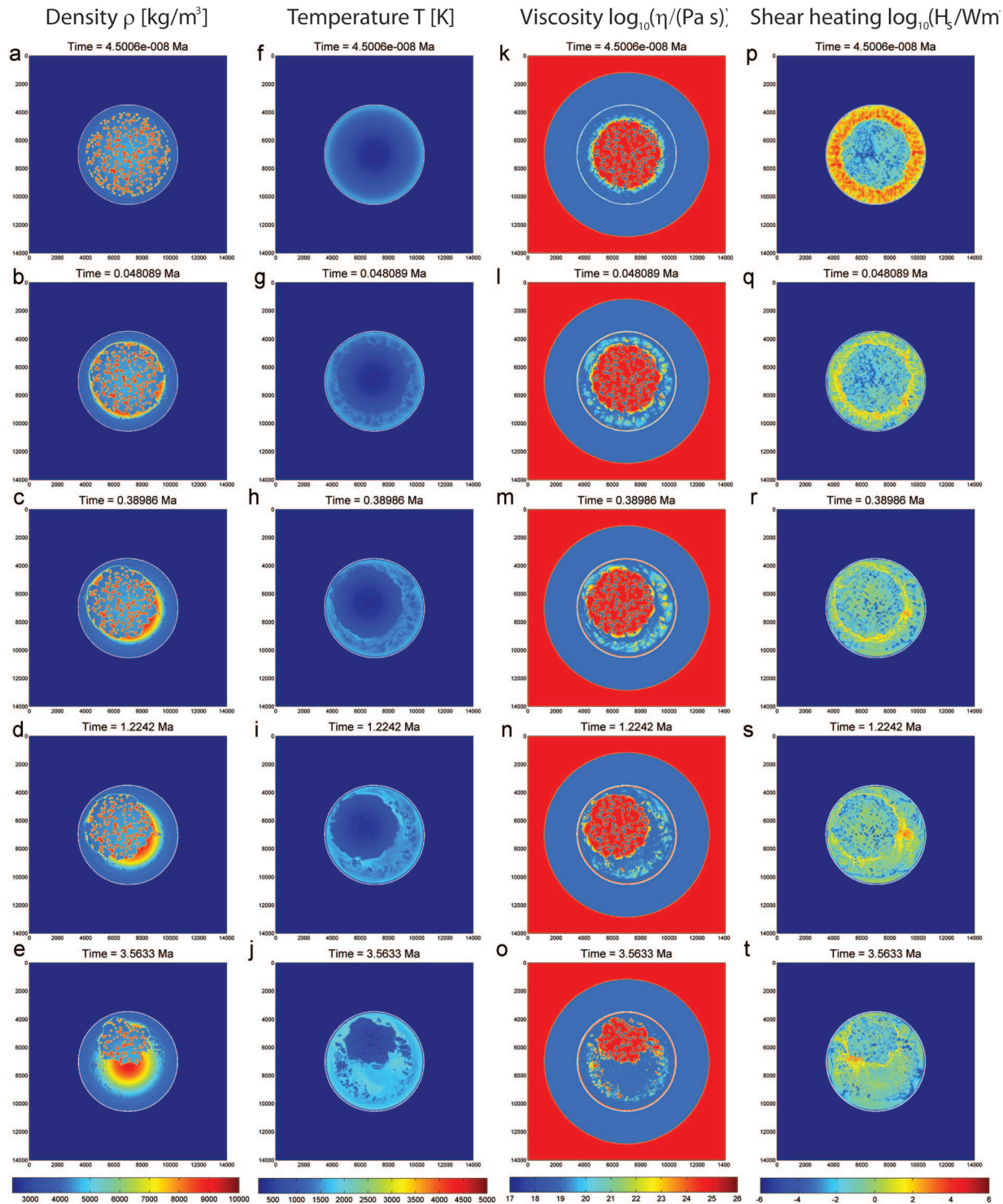
Figure 12. Same configuration as in Figure 7 but showing a case with $V_a = 8 \cdot 10^{-6}$ m³/mol, sin i = 0.6, and σ_P = $9.1 \cdot 10^9$ Pa, which depicts an example for the decomposition mechanism observed on a Mars-sized planetary embryo when applying a temperature profile with a cold central region (see equation (13)). Note that the scales are the same as in Figure 7 except that a lower visualization cutoff for density fields is used. Animations S15−S18 in the auxiliary material show the decomposition mode.

[54] The decomposition mode is illustrated in Figure 12 and was only observed in the following models: on Mars-sized planetary embryos with a cold central region employing dry olivine rheology ($\sigma_P = 9.1 \cdot 10^9$ Pa).

[55] In this mode the inner region of the planetary body is too stiff to allow the development of shear heating instabilities and/or plastic yielding of the silicate material. The iron diapirs sink with negligible velocities as Stokes spheres through the highly viscous medium of the central region and basically appear "frozen" (see Figure 12). In the hot outer layers the iron separates rapidly via collective diapirism (see section 5.1.1). The iron collects at the boundary between both areas and forms iron ponds around the central region. As the iron diapir distribution is initially random, the deviatoric stress created by these ponds is irregular and the central region is pushed out from the center of the planetary body as a large Stokes sphere, as suggested by *Elsasser* [1963], *Stevenson* [1981], *Ida et al.* [1987], *Honda et al.* [1993], and *Lin et al.* [2009]. When this stiff central region is decompressed as it approaches the surface of the planetary body, it decomposes into iron and silicates and core-mantle separation is completed afterward.

6. Scaling Analysis

[56] Our results indicate that under different rheological parameters iron diapirs show a diverse sinking behavior and that strong temperature variations inside a planetary body can foster the simultaneous existence of distinct core formation modes in different regions of a planetary body. Our observations indicate that plastic yielding and shear localization are important factors and control which core formation mode is active under given conditions. To get a better understanding of the diversity of diapir behaviors, we will focus in this section on a simple model, in which we study the behavior of a single diapir in a viscoplastic medium. We derive simplified scaling laws for the onset of plastic yielding and shear heating localization and test whether the analytical predictions fit the numerical models. Finally, we compare the scaling relationships with our full numerical models presented in section 5.

6.1. Development of Shear Localization

[57] Shear heating localization phenomena are important when heat is generated faster than it is conducted away and the local increase in temper-

ature and strain rate is strongly amplified [*Kaus*, 2005; *Kaus and Podladchikov*, 2006]. In 1-D this condition is given by:

$$\rho c_P \kappa \frac{\partial^2 \Delta T}{\partial x^2} \leq \sigma \dot{\varepsilon}, \tag{15}$$

where ρ is the density of the surrounding medium, κ is the thermal diffusivity, and $\Delta T = T - T_0$ is a small difference between actual temperature T and initial temperature T_0.

[58] We obtain the following relationship between the minimum radius r_{Fe} of an iron diapir needed to induce shear heating instabilities and the effective rheology of the surrounding medium (see Appendix B):

$$r_{Fe} \geq \left(\frac{f_1 c_P \kappa \eta_0}{\gamma \rho^n \left(\frac{8}{3} \pi G R_P \Delta \rho \right)^{n+1}} \right)^{\frac{1}{3+n}}, \tag{16}$$

where η_0 is the initial viscosity of the surrounding medium at temperature T_0, γ is the *e*-fold length of viscosity [*Turcotte and Schubert*, 2002], $\Delta \rho$ is the density difference between iron and silicate material and R_P is the radius of the planetary body. f_1 ($\sim 8^{3+n}$) is a factor accounting for the differences between analytical and numerical models. For the derivation of this formula, see Appendix B.

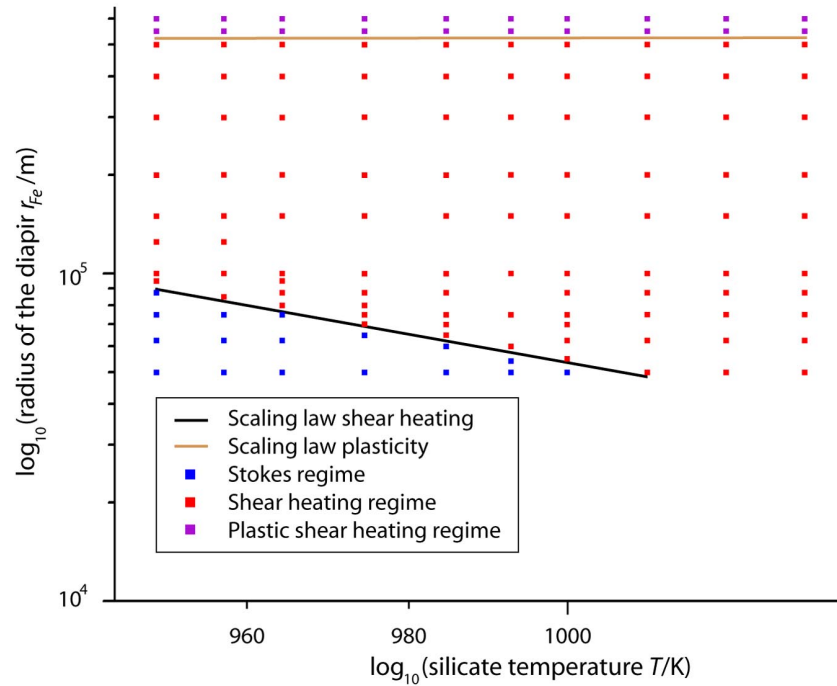## 6.2. Development of Plastic Yielding

[59] Plastic yielding becomes important when the deviatoric stress generated by the sinking iron diapir is comparable to the Peierls stress σ_P of the silicate medium. The minimum diapir radius r_{Fe} to induce plastic yielding can therefore be approximated as (for derivation see Appendix C):

$$r_{Fe} \geq \frac{3\sigma_P}{8\pi \rho \Delta \rho G R_P f_2} \tag{17}$$

f_2 (~ 0.1) is again a factor to convert between analytical and numerical results.

6.3. Numerical Test of the Scaling Law

[60] Here we use the simplified model described in section 3.2, where a single diapir sinks through a viscoplastic medium, to test the scaling laws. Because in the global models, several of the mechanisms tend to form larger iron ponds or collective groups of iron diapirs, we explore the influence of the diapir radius r_{Fe} and temperature in these models. A typical result from this model

Figure 13. Comparison between analytical and simplified numerical results on the development of plastic and shear heating effects dependent on silicate temperature T and diapir radius r_{Fe}. It can be seen that there are distinct regions in the diagram. Numerically, we can confirm a Stokes regime for small diapir in a cold medium, where neither plastic yielding nor shear localization occur. The shear heating regime is dominant for small diapirs in higher-temperature silicate material, and finally, the plastic shear heating regime is dominant for large diapirs in a warm medium.

is given in Animations S1 and S2 described in Appendix D.[1]

[61] The mean sinking velocity of the iron diapir is measured for cases with and without shear heating and for cases with plastic yielding included in order to estimate the importance of the different effects after the diapirs sink the same scaled distance

$$a = s/r_{Fe}, \quad (18)$$

where s is the dimensional sinking distance and r_{Fe} is the radius of the iron diapir. We chose a value of $a = 0.01$ for our experiments.

[62] To discriminate between the different regimes we define the ratios

$$r_1 = \frac{v_{Hs}}{v_{w/o}} - 1 \quad (19a)$$

and

$$r_2 = \frac{v_{pl}}{v_{w/o}} - 1, \quad (19b)$$

where v_{Hs} is the sinking velocity of the iron diapir measured when accounting for shear heating, $v_{w/o}$ is the velocity observed when both shear heating and plasticity are not taken into account and v_{pl} is the velocity when considering plasticity.
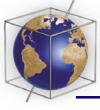
[63] To discriminate between the different regimes we use values of r_1 and r_2 of $\geq 3.5 \cdot 10^{-2}$. When we choose proper factors f_1 ($\sim 8^{3+n}$) and f_2 (~ 0.1) to account for the differences between the analytical and numerical models, we find a good agreement between the analytical predictions and the numerical results (see Figure 13).

[64] Next we compare the results of the scaling laws with our different core formation regimes observed in the planet-scale models of section 5. We take typical values for temperature and the radius of a diapir or iron pond from typical results, as seen in Figures 7–10 and 12 (see Figure 14).

6.3.1. Collective Diapirism

[65] For the collective diapirism mode we observe (see Figures 7 and 14a) that in different regions of the planetary body all 4 regimes prevail: Large collective groups can activate both plastic yielding and shear heating instabilities, whereas small iron diapirs in cold near-surface regions with a small
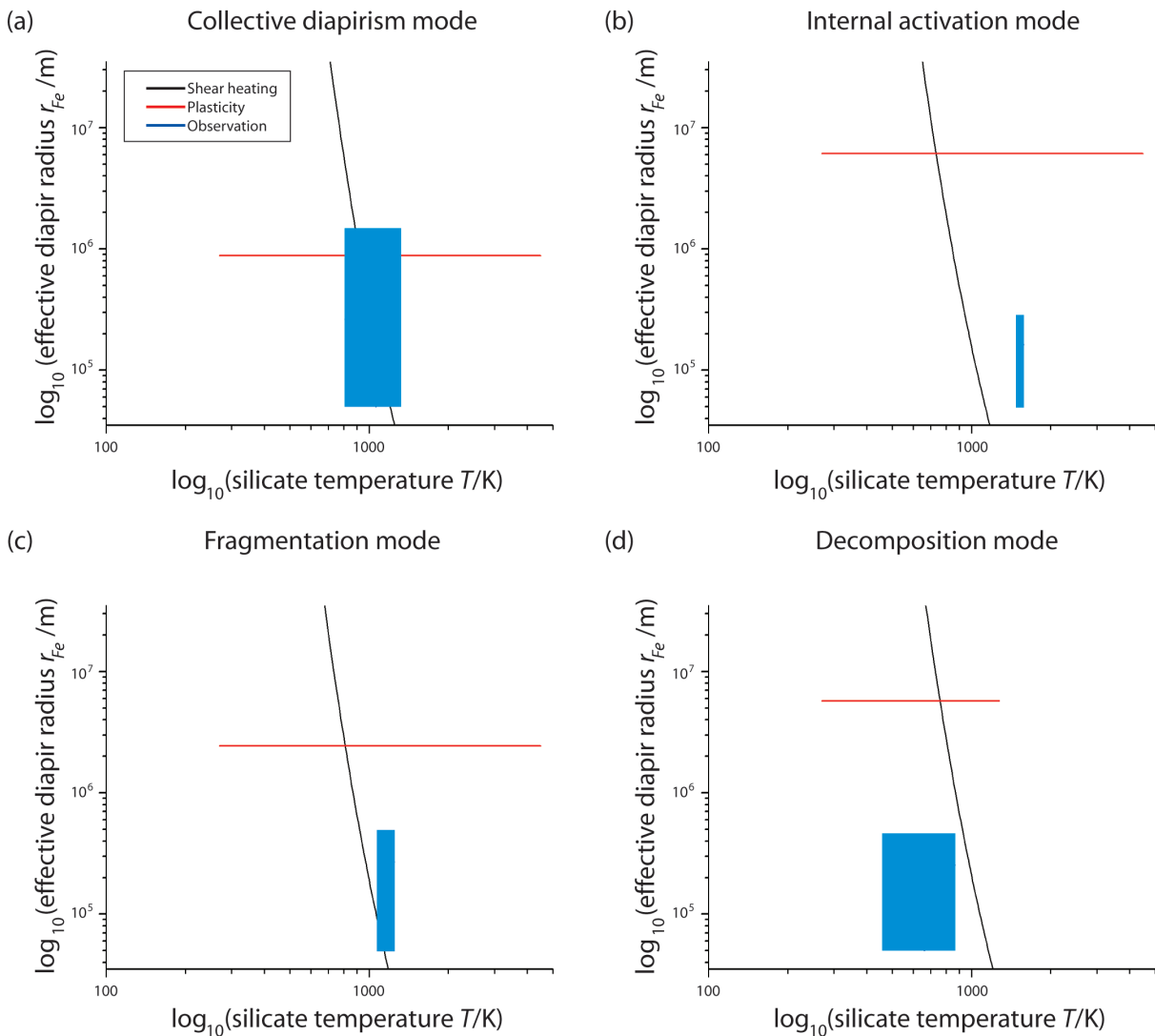
Figure 14. Comparison between the scaling laws using parameters as given in the particular model and observations of typical values for diapir and iron pond radii and silicate temperatures for (a) the collective diapirism mode, (b) the internal activation mode, (c) the fragmentation mode, and (d) the decomposition mode.

iron/silicate ratio are not able to activate either plastic yielding or shear heating localization and are therefore trapped until these regions are significantly heated. Equations (16) and (17) indicate that on large Earth-sized protoplanets with a weak rheology, shear localization and plastic yielding can be more easy activated by the same diapirs than on a smaller Mars-sized planetary embryo, which is in agreement with appearance of the collective diapirism mode (see Figures 5a and 5b).

6.3.2. Internal Activation Mode

[66] The internal activation mode (see Figures 8 and 14b) can be explained as follows: A strongly temperature-dependent, however only weakly pressure-dependent rheology is required for the internal

activation mode. In the inner regions, large temperatures occur, such that most of the iron diapirs are able to induce shear heating instabilities, which help to induce fast core segregation (see equation (16)). The cold exterior shell will be initially in the Stokes mode as the rheology in this case is largely dominated by the temperature field. Once the upwelling plumes produce enough deviatoric stress and/or radioactive decay increases its temperature, shear heating instabilities may develop, which slice the outer shell into distinct fragments.

6.3.3. Fragmentation Mode

[67] Equation (16) indicates that very large iron diapirs are required to yield a highly viscous material (as occurs for strongly pressure-dependent
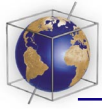
rheologies). Once radiogenic heating is taken into account this threshold will decrease very rapidly with time, as viscosity is temperature-dependent. As equation (16) is also highly dependent to the distance from the center of the body, shear heating is expected to be first activated in the outer shell of such a body (see Figure 9 and 10). With increasing depth, the pressure rises and larger temperatures are needed to reduce the viscosity to a level where shear heating instabilities can develop. Additionally, the distance to the planetary center is smaller, therefore shear heating instabilities can develop in deeper regions later and/or need larger iron ponds to induce shear heating. This agrees with our observations made for the fragmentation mode (see Figure 14c).

6.3.4. Decomposition Mode

[68] Under the extreme conditions of a dry rheology (large σ_P), a small radius R_P of the planetary body and low internal temperature T, neither plastic yielding nor shear heating instabilities can develop (see equations (16) and (17) and Figures 12 and 14d). Under these conditions, diapir propagation is only possible via Stokes sinking until the temperature rises significantly. When the outer regions are hot, shear heating instabilities can develop there, which quickly result in iron ponds or an iron layer around the central region. When the deviatoric stress created by such ponds is insufficient to yield the central layer, the central layer will behave as a large sphere, which is pushed out of the center of the planet. Once the central region decompresses, its viscosity will drop significantly and shear localization can develop and/or the central region will decompose in silicates and iron as was observed in our decomposition mode.

7. Discussion

[69] We observe four core formation modes in our numerical models:

[70] 1. Collective iron diapirism requires the entire planetary body to be relatively weak (low viscosity). The bulk of core formation happens via plastic yielding and shear localization.

[71] 2. Internal activation is observed for all cases with a low activation volume, hence weak interior and strong outer shell, and leads to fast differentiation of the central region of the body via shear localization.

[72] 3. The fragmentation mode is dominant for stiff rheologies and the main characteristic of this mode is shear localization confined to narrow shear bands, which move from the outside to the interior of the planetary body.
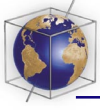
[73] 4. In the decomposition mode, under extreme cases, neither plastic yielding nor shear localization will occur. In these cases, the stiff central region behaves as a large Stokes sphere that is pushed out from the center by sinking iron.

[74] All models indicate core formation times of less than 20 Ma, which is broadly in agreement with both geochemical [e.g., *Halliday*, 2008; *Allègre et al.*, 2008] and numerical results [e.g., *Chambers*, 2004] for planetary accretion and differentiation and support the idea of simultaneous accretion and differentiation of accreting planetary bodies, and allows for episodic differentiation of an accreting planetary body.

[75] Our main models and scaling laws indicate that core formation times are dependent on the activation volume V_a, the Peierls stress σ_P, and the temperature state of the protoplanetary body as well as the radius of the iron diapirs r_{Fe}. Friction angle only has an influence if it is extremely small ($\sin i < 0.05$). These rheological parameters are able to shift the boundaries between different regimes and foster a faster differentiation process (see Figure 15). Therefore in different regions of an accreting planet with certain silicate temperature and pressure conditions distinct core formation mechanisms will prevail. With our current knowledge, it seems feasible that all the described modes could have been active during some stage of core formation.

7.1. Influence of Water on the Differentiation Process

[76] On Mars-sized planetary embryos the effect of water on the rheology is only marginal. Its effect is limited to the time scale of core formation as it reduces the viscosity of the material, but it has no significant effect on the core formation mode. During the later stages (i.e., for a larger protoplanet), however, different evolutionary paths are distinguishable: For weak olivine rheologies, collective diapirism and internal activation are the dominant core formation modes on Earth-sized protoplanets (see Figure 5). In contrast, on planetary bodies with stiff olivine rheologies the fragmentation mode might still prevail during the late stages of core formation.
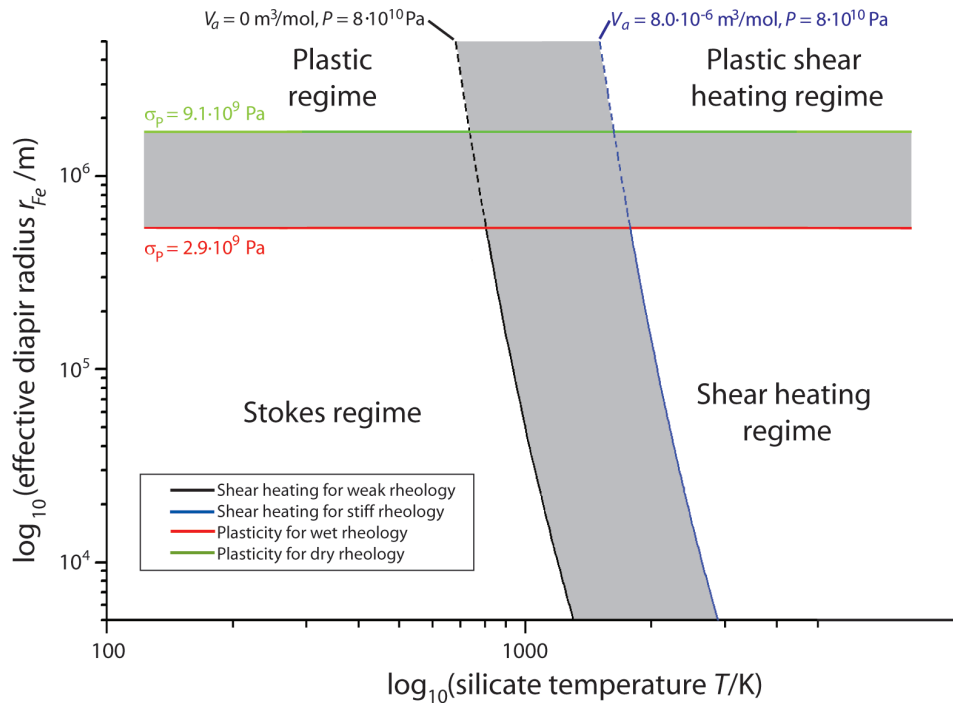
Figure 15. Boundaries between the different physical regimes for an Earth-sized protoplanet employing a pressure-independent (black curve) and a strongly pressure-dependent silicate rheology (blue curve) (see equation (16)). The red and green curves give the yield radii for wet and dry olivine rheology (see equation (17)). As shown by the shaded region the rheological parameters can shift the boundaries between the different regimes. Therefore the areas dominated by a certain core formation mode as shown in Figure 5 are shifted as well due to water presence.

[77] At the current knowledge both wet or dry models may be applicable as the timing of water insertion into the terrestrial planets is still debated: While *Boss* [1998] proposes a hot accretion disk and late addition of water by comets and meteorites, *Drake* [2005] and *Muralidharan et al.* [2008] discuss an early absorption of water by silicate grains prior to planetary accretion. They show that the volume of several Earth oceans could be stored even under high temperatures in the silicate grains. Results by *Morbidelli et al.* [2000], *Raymond et al.* [2007], and *Bond et al.* [2009], on the other hand, indicate that the most important source of water delivery to the growing Earth-sized protoplanet is the accretion of hydrated planetesimals and planetary embryos coming from the outer asteroid belt. This mechanism starts at $\sim 10^7$ years after the start of the solar system as the early formed giant planets [e.g., *Pollack et al.*, 1996; *Hubickyj*, 2006; *Lissauer et al.*, 2009] deplete the primordial asteroid belt [*Wetherill*, 1992; *Chambers and Wetherill*, 1998, 2001; *Petit et al.*, 2001; *O'Brien et al.*, 2007; *Minton and Malhotra*, 2009], which coincides with the oligarchic growth stage of the terrestrial protoplanets [e.g., *Kokubo and Ida*, 2000; *Chambers*, 2004]. It is expected that during this stage the mass of a growing protoplanet

should be around half of the Earth's present mass [*Morbidelli et al.*, 2000]. For further possible mechanisms of water delivery to the terrestrial planets see *Drake* [2005]. Therefore, the models presented here might represent end-members of a dry accretion or a generally wet accretion history of a terrestrial planet.

[78] Temperature profiles throughout the differentiating planetary body give some constraints on the possible existence of a basal magma ocean [*Labrosse et al.*, 2007] and the thermal state of the core on the early terrestrial planetary bodies. Drastic temperature differences occur between the different core formation mechanisms. In Figures 16a–16d typical examples of temperature profiles for different core formation modes both in Mars-sized planetary embryos (Figures 16a and 16b) and Earth-sized protoplanets (Figures 16c and 16d) are given. Both the internal activation mode dominant on a weak Mars-sized planetary embryo (Figure 16a) and the collective diapirism mode (Figure 16c) in a weak Earth-sized protoplanet show a hot lower mantle, whereas the core itself is rather cool. The highest mean temperatures are observed close to the core mantle boundary. The fragmentation cases for a Mars-sized planetary
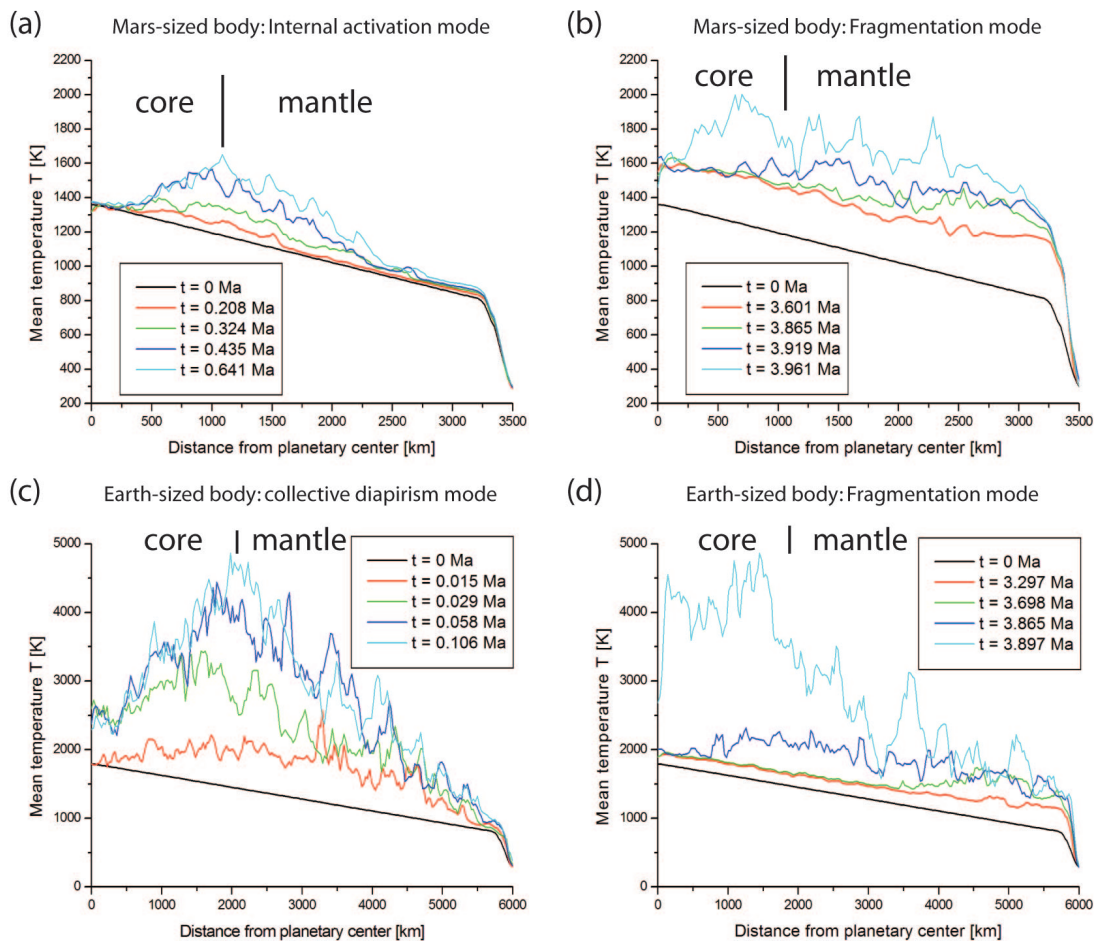
Figure 16. Average temperature profiles for different time steps and for different regimes, for both (a and b) Mars-sized and (c and d) Earth-sized models. Figures 16a and 16c show results for the internal activation and collective diapirism mode, whereas Figures 16b and 16d represent cases where the fragmentation mode is active. The average temperatures were determined from radial temperature profiles ranged from the center of the planetary body to 3500 km (Mars-sized planetary embryo) and 6000 km (Earth-sized protoplanet) radius. These radial profiles were taken in 30° intervals, and the arithmetic mean of the resulting 11 profiles was computed. Note that due to the aspherical deformation of the planetary body, temperatures given at 3500 or 6000 km radii must not correspond with the surface of the planetary body.

embryo (Figure 16b) and an Earth-sized protoplanet (Figure 16d) show similar mean mantle temperatures of around 1800 to 2000 K, however the core seems to be almost equally hot (in the case of Mars-sized planetary embryo) or in the case of an Earth-sized body, significantly superheated ($\Delta T >$ 1500 K). The temperature differences between the two different sized planetary bodies can be attributed to the different amounts of potential energy released [*Schubert et al.*, 1986]. The comparison of shear heating for these different modes (see Figures 7–10) shows that in the case of collective diapirism, shear heating is small inside the collective group. Therefore some iron material will stay cooler, which results in a generally cooler iron core, whereas the lower mantle may reach temperatures high enough to support silicate melting as

most of the silicate material experiences significant shear heating. A similar temperature profile for core formation via sinking diapirs on a Mars-sized body was obtained by H. Samuel and P. J. Tackley (Heat partitioning in terrestrial planets during core formation by negative diapirism, submitted to *Earth and Planetary Science Letters*, 2009). This may result in the formation of a basal magma ocean as suggested by *Labrosse et al.* [2007]. In the fragmentation mode, on the contrary, most of the iron is thinned during the core formation process and encounters strong shear heating. Our results are in agreement with recent work by *Ke and Solomatov* [2009], who argued using simple scaling laws that the manner in which iron moves though the silicate mantle controls the energy partitioning between mantle and core. They argued

that sinking iron diapirs, as occur in our collective diapirism mode, dissipate gravitational energy in the mantle, whereas iron channels, as are observed in the fragmentation mode, tend to transport most of the energy to the core. The result is an initially superheated iron core as described by *Ke and Solomatov* [2006, 2009] and *Stevenson* [2001, 2008]. These two different evolutionary paths may have significant implications for the onset of mantle convection and the geodynamo.

7.2. Model Limitations

[79] It should be noted that temperature profiles and other aspects of our results are influenced by the following model assumptions: That a large fraction of the iron is sinking simultaneously and in relatively large diapirs, and that the initial temperature profile throughout the forming planetary bodies ignores the effects of earlier episodes of core formation. In our model, only simple temperature profiles have been applied, whereas real profiles could have been much more complex and are dependent on the accretion history of a body [e.g., *Sleep*, 2000]. This is confirmed by results for accreting planetesimals by *Merk et al.* [2002], *Ghosh et al.* [2003], *Hevey and Sanders* [2006], and *Sahijpal et al.* [2007]. Future research should therefore focus on the investigation of possible temperature profiles for growing terrestrial planetary bodies, as the temperature profile is a key parameter controlling the rheological state of an accreting planetary body (see also Figure 15). On the other hand, the actual diapir size distribution might be very broad, with most diapirs having significantly smaller radii than in our calculations. Therefore, the temperatures obtained in our models should be considered as an upper limit. Higher-resolution models are required in the future to allow for the proper resolution of smaller diapirs than included here in our global differentiation models.

[80] An additional simplification is that we applied for both wet and dry olivine rheology the same values for the preexponential parameter A, the activation energy E_a and the power law coefficient n (for dry olivine) and overestimated the effective viscosity of the silicate medium in cases considering wet olivine rheology. An additional model analog to the model shown in Figure 7, however considering these parameters (see Table 1 for the numbers employed) is shown in Appendix E.

[81] Finally, our study ignores the effects of phase transitions, which might be important in Earth-sized terrestrial protoplanets because their mantles consist mostly of perovskite, which has a lower activation energy and activation volume [*Yamazaki and Karato*, 2001; *Ammann et al.*, 2009] than olivine. This could favor the core formation modes observed for weak rheologies in planetary bodies with significant amounts of perovskite. These aspects will be explored in more detail in a future study.

8. Conclusions

[82] Our results show that the application of a great number of sinking iron diapirs and non-Newtonian rheology results in several core formation mechanisms, which differ significantly from previous numerical results in which only a single diapir was modeled. Silicate rheology controls the mode of core formation experienced by the accreting planetary bodies. Plastic yielding– and shear heating–related effects result in significantly shorter core formation times than suggested by previous models employing Newtonian rheology, as they lead to positive feedbacks. For Earth-sized terrestrial protoplanets the water content can have a significant influence on the prevailing core formation mode as it changes the Peierls stress significantly. Generally the results show that due to the dependency of viscosity on parameters as pressure, temperature, and strain rate even planetary bodies with a hot interior can be highly viscous, which was ignored in previous studies. The different core formation modes observed result in significantly different temperature profiles through the differentiated planetary bodies, which may have an influence on the onset of the geodynamo and mantle convection.

Appendix A

[83] In Figure S1 shear heating patterns for comparable time steps are shown for three different grid resolutions: 501×501, 1001×1001 and 1401×1401 nodal points. It can be seen that the general pattern is properly resolved with the grid containing 501 nodal points.

Appendix B

[84] To initialize shear localization the following condition has to be met in the diffusion equation [e.g., *Kaus and Podladchikov*, 2006]:

$$f_1 c_P \rho \kappa \frac{\partial^2 \Delta T}{\partial x^2} \leq \sigma \dot{\varepsilon}, \qquad (B1)$$

where ρ is the density of the surrounding medium, κ is the thermal diffusivity, c_P is the specific heat capacity, and $\Delta T = T - T_0$ is the small difference between actual temperature T and initial temperature T_0 in the surrounding medium. σ represents the stress tensor and $\dot{\varepsilon}$ is the strain rate tensor. f_1 is a factor which accounts for the discrepancy between numerics and analytics.

[85] We apply the Frank-Kamenetzkii approximation [*Frank-Kamenetzkii*, 1969]:

$$\dot{\varepsilon} = \frac{1}{\eta_0} \exp(\gamma \Delta T)\sigma_0^n, \tag{B2}$$

where η_0 is the "viscosity" for temperature T_0 and is given as $\eta_0 = A \exp[(E_a + PV_a)/RT_0]$, where A is the preexponential parameter, E_a is the activation energy, P is the pressure, V_a is the activation volume and R is the universal gas constant. γ is the e-fold length of the viscosity [*Turcotte and Schubert*, 2002], n is the power law coefficient and σ_0 is the deviatoric stress.

[86] As the temperature difference ΔT is small, we use a Taylor expansion and truncate after the linear term: $\exp(\gamma \Delta T) \approx 1 - \gamma \Delta T$

[87] Inserting (B2) and the result of the Taylor expansion into (B1) and discretizing the equation by replacing $\frac{\partial^2 \Delta T}{\partial x^2}$ by $\frac{\Delta T}{r_{Fe}^2}$, where r_{Fe} is the size of the inhomogeneity, which is in our case the radius of the iron diapir [see also *Kaus and Podladchikov*, 2006] yields:

$$f_1 c_P \rho \kappa \frac{\Delta T}{r_{Fe}^2} \leq \frac{\gamma \Delta T \sigma_0^{n+1}}{(1 + \gamma \Delta T)\eta_0} \tag{B3}$$

Using equation (B3) it is now possible to derive an expression for the minimum radius of a diapir r_{Fe} needed to induce shear localization inside an accreting planetary body.

[88] The deviatoric stress created by a diapir of radius r_{Fe} can be approximated with the following expression:

$$\sigma_0 = 2r_{Fe}\Delta\rho g, \tag{B4}$$

where $\Delta\rho$ is the density difference between the inhomogeneity and the surrounding medium and g is the gravity acceleration.

[89] After introducing equation (B4) into (B3) we get:

$$r_{Fe} \geq \left(\frac{f_1 \rho c_P \kappa \eta_0}{\gamma(2\Delta\rho g)^{n+1}}\right)^{1/(3+n)} \left(\frac{\Delta T}{1 + \gamma \Delta T}\right)^{1/(3+n)} \tag{B5}$$

For a small temperature difference ΔT and using values for γ and n as given in Table 1, the term $\left(\frac{\Delta T}{1 + \gamma \Delta T}\right)^{1/(3+n)}$ is ~ 1 and can be neglected.

[90] The gravitational acceleration g at the surface of a homogeneous planetary body is:

$$g = \frac{4}{3}\pi\rho G R_P, \tag{B6}$$

where G is the gravitational constant and R_P is the radius of the planetary body.

[91] The final result is:

$$r_{Fe} \geq \left(\frac{f_1 c_P \kappa \eta_0}{\gamma \rho^n \left(\frac{8}{3}\pi G R_P \Delta\rho\right)^{n+1}}\right)^{\frac{1}{3+n}} \tag{B7}$$

Appendix C

[92] We approximate the deviatoric stress σ_0 created by the inhomogeneity (the iron diapir) as described above in (B4) and set it equal to the Peierls stress σ_P, which we assume to be constant in our models. Additionally we use (B6) to describe the gravitational acceleration and get as the final result

$$r_{Fe} \geq \frac{3\sigma_P}{8\pi\rho\Delta\rho G R_P f_2}, \tag{C1}$$

where f_2 is the factor accounting for the discrepancy between numerical results and analytical theory.

Appendix D

[93] Shown are two movies with results for the simplified simulations performed using MILAMIN_VEP, which we used to derive the scaling law. In both movies the transient evolution of the following six fields is shown, which are from top left to down right: Logarithm of the second invariant of strain rate tensor, Logarithm of the shear viscosity, Second invariant of the stress tensor, temperature, vertical velocity and the sinking velocity of the iron diapir.

[94] In these models, an iron diapir with 200 km radius is assumed and in Animation S1 shear heating is taken into account whereas Animation S2 shows a run without shear heating. The remaining physical parameters of the model can be found in Table 1. It can be seen that the case without shear heating reaches very quickly its terminal

velocity, whereas in the case with shear heating included the sinking velocity of the iron diapir increases with time.

Appendix E

[95] To estimate the influence of the preexponential parameter A, the activation energy E_a and the power law coefficient n for wet olivine rheology, we performed an additional experiment using values for these parameters as suggested by *Ranalli* [1995] (see also Table 1 for the employed numbers). The same setup is used for Figure S2 as in Figure 7 is used and similar time steps as in Figure 7 are shown. It can be seen that the general pattern of development is similar, however the time scale of differentiation in the wet model is shorter.

Acknowledgments
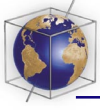
References

Abe, Y. (1997), Thermal and chemical evolution of the terrestrial magma ocean, *Phys. Earth Planet. Inter.*, *100*, 27–39, doi:10.1016/S0031-9201(96)03229-3.

Agnor, C. B., R. M. Canup, and H. F. Levison (1999), On the character and consequences of large impacts in the late stage of terrestrial planet formation, *Icarus*, *142*, 219–237, doi:10.1006/icar.1999.6201.

Allègre, C. J., G. Manhès, and C. Göpel (2008), The major differentiation of the Earth ∼4.45 Ga, *Earth Planet. Sci. Lett.*, *267*, 386–398, doi:10.1016/j.epsl.2007.11.056.

Ammann, M. W., J. P. Brodholt, and D. P. Dobson (2009), DFT study of migration enthalpies in MgSiO₃ perovskite, *Phys. Chem. Miner.*, *36*, 151–158, doi:10.1007/s00269-008-0265-z.

Asphaug, E., C. B. Agnor, and Q. Williams (2006), Hit-and-run planetary collisions, *Nature*, *439*, 155–160, doi:10.1038/nature04311.

Barr, A. C., and R. M. Canup (2008), Constraints on gas giant satellite formation from the interior states of partially differentiated satellites, *Icarus*, *198*, 163–177, doi:10.1016/j.icarus.2008.07.004.

Bond, J. C., D. S. Lauretta, and D. P. O'Brien (2009), Making the Earth: Combining dynamics and chemistry in the solar system, *Icarus*, doi:10.1016/j.icarus.2009.07.037, in press.

Boss, A. P. (1998), Temperatures in protoplanetary disks, *Annu. Rev. Earth Planet. Sci.*, *26*, 53–80, doi:10.1146/annurev.earth.26.1.53.

Breuer, D., and W. B. Moore (2007), Dynamics and thermal history of the terrestrial planets, the Moon, and Io, in *Treatise on Geophysics*, vol. 10, *Planets and Moons*, edited by T. Spohn, pp. 299–348, Elsevier, Amsterdam.

Carlson, R. W., and G. W. Lugmair (2000), Timescales of planetesimal formation and differentiation based on extinct and extant radioisotopes, in *Origin of the Earth and Moon*, edited by R. M. Canup and K. Righter, pp. 25–44, Ariz. Univ. Press, Tucson.

Chambers, J. E. (2004), Planetary accretion in the inner solar system, *Earth Planet. Sci. Lett.*, *223*, 241–252, doi:10.1016/j.epsl.2004.04.031.

Chambers, J. E., and G. W. Wetherill (1998), Making the terrestrial planets: N-body integrations of planetary embryos in three dimensions, *Icarus*, *136*, 304–327, doi:10.1006/icar.1998.6007.

Chambers, J. E., and G. W. Wetherill (2001), Planets in the asteroid belt, *Meteorit. Planet. Sci.*, *36*, 381–399.

Dahl, T. W. (2005), Turbulent mixing during planet accretion and core formation: Interpretation of the Hf/W chronometer and implications for the age of the Moon, M.S. thesis, 127 pp., Univ. of Copenhagen, Copenhagen.

Davies, G. F. (1985), Heat deposition and retention in a solid planet growing by impacts, *Icarus*, *63*, 45–68, doi:10.1016/0019-1035(85)90020-X.

Day, J. M. D., R. D. Ash, Y. Liu, J. J. Bellucci, D. Rumble III, W. F. McDonough, R. J. Walker, and L. A. Taylor (2009), Early formation of evolved asteroidal crust, *Nature*, *457*, 179–182, doi:10.1038/nature07651.

Drake, M. J. (2005), Origin of water in the terrestrial planets, *Meteorit. Planet. Sci.*, *40*, 1–9.

Elsasser, W. M. (1963), Early history of the Earth, in *Earth Science and Meteoritics*, edited by J. Geiss and E. Goldberg, pp. 1–30, North-Holland, Amsterdam.

Evans, B., and C. Goetze (1979), The temperature variation of hardness of olivine and its implication for polycrystalline yield stress, *J. Geophys. Res.*, *84*, 5505–5524, doi:10.1029/JB084iB10p05505.

Evonuk, M., and G. A. Glatzmaier (2006), A 2D study of the effects of the size of a solid core on the equatorial flow in giant planets, *Icarus*, *181*, 458–464, doi:10.1016/j.icarus.2005.12.004.

Frank-Kamenetzkii, D. A. (1969), *Diffusion and Heat Transfer in Chemical Kinetics*, 574 pp., Plenum, New York.

Frenkel, J. (1926), Zur Theorie der Elastizitätsgrenze und der Festigkeit kristallinischer Körper, *Z. Phys.*, *37*, 572–609, doi:10.1007/BF01397292.

Gerya, T. V., and D. A. Yuen (2003), Characteristics-based marker-in-cell method with conservative finite-differences schemes for modeling geological flows with strongly variable transport properties, *Phys. Earth Planet. Inter.*, *140*, 293–318, doi:10.1016/j.pepi.2003.09.006.

Gerya, T. V., and D. A. Yuen (2007), Robust characteristics method for modelling multiphase visco-elasto-plastic thermo-mechanical problems, *Phys. Earth Planet. Inter.*, *163*, 83–105, doi:10.1016/j.pepi.2007.04.015.

Ghosh, A., S. J. Weidenschilling, and H. Y. McSween Jr. (2003), Importance of the accretion process in asteroid thermal evolution: 6 Hebe as an example, *Meteorit. Planet. Sci.*, *38*, 711–724.

Golabek, G. J., H. Schmeling, and P. J. Tackley (2008), Earth's core formation aided by flow channelling instabilities in-

duced by iron diapirs, *Earth Planet. Sci. Lett.*, *271*, 24–33, doi:10.1016/j.epsl.2008.02.033.

Greenwood, R. C., I. A. Franchi, A. Jambon, and P. C. Buchanan (2005), Widespread magma oceans on asteroidal bodies in the early solar system, *Nature*, *435*, 916–918, doi:10.1038/nature03612.

Gutenberg, B. (1913), Über die Konstitution des Erdinnern, erschlossen aus Erdbebenbeobachtungen, *Phys. Z.*, *14*, 1217–1218.

Halliday, A. N. (2008), A young Moon-forming giant impact at 70–110 million years accompanied by late-stage mixing, core formation and degassing of the Earth, *Philos. Trans. R. Soc. A*, *366*, 4163–4181, doi:10.1098/rsta.2008.0209.

Hevey, P. J., and I. S. Sanders (2006), A model for planetesimal meltdown by ^{26}Al and its implications for meteorite parent bodies, *Meteorit. Planet. Sci.*, *41*, 95–106.

Höink, T., J. Schmalzl, and U. Hansen (2006), Dynamics of metal-silicate separation in a terrestrial magma ocean, *Geochem. Geophys. Geosyst.*, *7*, Q09008, doi:10.1029/2006GC001268.

Honda, R., H. Mizutani, and T. Yamamoto (1993), Numerical simulation of Earth's core formation, *J. Geophys. Res.*, *98*, 2075–2089, doi:10.1029/92JB02699.

Hubickyj, O. (2006), The core accretion-gas capture model for gas-giant planet formation, in *Planet Formation: Theory, Observations, Experiments*, edited by H. Klahr and W. Brandner, pp. 163–178, Cambridge Univ. Press, Cambridge, U. K.

Ida, S., Y. Nakagawa, and K. Nakazawa (1987), The Earth's core formation due to the Rayleigh-Taylor instability, *Icarus*, *69*, 239–248, doi:10.1016/0019-1035(87)90103-5.

Kameyama, M., D. A. Yuen, and S. Karato (1999), Thermal-mechanical effects of low-temperature plasticity (the Peierls mechanism) on the deformation of a viscoelastic shear zone, *Earth Planet. Sci. Lett.*, *168*, 159–172, doi:10.1016/S0012-821X(99)00040-0.

Karato, S., and V. R. Murthy (1997), Core formation and chemical equilibrium in the Earth I. Physical considerations, *Phys. Earth Planet. Inter.*, *100*, 61–79, doi:10.1016/S0031-9201(96)03232-3.

Katayama, I., and S. Karato (2008), Low-temperature, high-stress deformation of olivine under water-saturated conditions, *Phys. Earth Planet. Inter.*, *168*, 125–133, doi:10.1016/j.pepi.2008.05.019.

Kaus, B. J. P. (2005), Modelling approaches to geodynamic processes, Ph.D. thesis, 259 pp., Swiss Fed. Inst. of Technol., Zurich, Switzerland.

Kaus, B. J. P., and Y. Y. Podladchikov (2006), Initiation of localized shear zones in viscoplastic rocks, *J. Geophys. Res.*, *111*, B04412, doi:10.1029/2005JB003652.

Kaus, B. J. P., C. Steedman, and T. W. Becker (2008), From passive continental margin to mountain belt: Insights from analytical and numerical models and application to Taiwan, *Phys. Earth Planet. Inter.*, *171*, 235–251, doi:10.1016/j.pepi.2008.06.015.

Ke, Y., and V. S. Solomatov (2006), Early transient super-plumes and the origin of the Martian crustal dichotomy, *J. Geophys. Res.*, *111*, E10001, doi:10.1029/2005JE002631.

Ke, Y., and V. S. Solomatov (2009), Coupled core-mantle thermal evolution of early Mars, *J. Geophys. Res.*, *114*, E07004, doi:10.1029/2008JE003291.

Kokubo, E., and S. Ida (2000), Formation of protoplanets from planetesimals in the Solar Nebula, *Icarus*, *143*, 15–27, doi:10.1006/icar.1999.6237.

Kotelkin, V. D., and L. I. Lobkovsky (2007), The Myasnikov global theory of the evolution of planets and the modern thermochemical model of the Earth's evolution, *Izv. Phys. Solid Earth*, *43*, 24–41, doi:10.1134/S1069351307010041.

Labrosse, S., J. W. Hernlund, and N. Coltice (2007), A crystallizing dense magma ocean at the base of the Earth's mantle, *Nature*, *450*, 866–869, doi:10.1038/nature06355.

Lin, J.-R., T. V. Gerya, P. J. Tackley, D. A. Yuen, and G. J. Golabek (2009), Numerical modeling of protocore destabilization during planetary accretion: Methodology and results, *Icarus*, doi:10.1016/j.icarus.2009.06.035, in press.

Lissauer, J. J., O. Hubickyj, G. D'Angelo, and P. Bodenheimer (2009), Models of Jupiter's growth incorporating thermal and hydrodynamic constraints, *Icarus*, *199*, 338–350, doi:10.1016/j.icarus.2008.10.004.

Lodders, K., and B. Fegley (1998), *The Planetary Scientist's Companion*, 400 pp., Oxford Univ. Press, New York.

MacPherson, G. J., A. M. Davis, and E. K. Zinner (1995), The distribution of aluminium-26 in the early Solar system—A reappraisal, *Meteoritics*, *30*, 365–386.

Mei, S., and D. L. Kohlstedt (2000a), Influence of water on plastic deformation of olivine aggregates: 1. Diffusion creep regime, *J. Geophys. Res.*, *105*, 21,457–21,469, doi:10.1029/2000JB900179.

Mei, S., and D. L. Kohlstedt (2000b), Influence of water on plastic deformation of olivine aggregates: 2. Dislocation creep regime, *J. Geophys. Res.*, *105*, 21,471–21,481, doi:10.1029/2000JB900180.

Melosh, H. J. (1990), Giant impacts and the thermal state of the early Earth, in *Origin of the Earth*, edited by H. E. Newsom and J. H. Jones, pp. 69–83, Oxford Univ. Press, New York.

Merk, R., D. Breuer, and T. Spohn (2002), Numerical modeling of ^{26}Al-induced radioactive melting of asteroids considering accretion, *Icarus*, *159*, 183–191, doi:10.1006/icar.2002.6872.

Minton, D. A., and R. Malhotra (2009), A record of planet migration in the main asteroid belt, *Nature*, *457*, 1109–1111, doi:10.1038/nature07778.

Moll, G.-P., G. J. Golabek, and T. V. Gerya (2009), Influence of giant impactors on the terrestrial core formation, *Geophys. Res. Abstr.*, *11*, Abstract EGU2009-5460.

Morbidelli, A., J. Chambers, J. I. Lunine, J. M. Petit, F. Robert, G. B. Valsecchi, and K. E. Cyr (2000), Source regions and time scales for the delivery of water to the Earth, *Meteorit. Planet. Sci.*, *35*, 1309–1320.

Moresi, L., F. Dufour, and H.-B. Mühlhaus (2003), A Lagrangian integration point finite element method for large deformation modeling of viscoelastic geomaterials, *J. Comput. Phys.*, *184*, 476–497, doi:10.1016/S0021-9991(02)00031-1.

Muralidharan, K., P. Deymier, M. Stimpfl, N. H. de Leeuw, and M. J. Drake (2008), Origin of water in the inner Solar System: A kinematic Monte Carlo study of water absorption on forsterite, *Icarus*, *198*, 400–407, doi:10.1016/j.icarus.2008.07.017.

O'Brien, D. P., A. Morbidelli, and W. F. Bottke (2007), The primordial excitation and clearing of the asteroid belt—Revisited, *Icarus*, *191*, 434–452, doi:10.1016/j.icarus.2007.05.005.

Olson, P., and D. S. Weeraratne (2008), Experiments on metal-silicate plumes and core formation, *Philos. Trans. R. Soc. A*, *366*, 4253–4271, doi:10.1098/rsta.2008.0194.

Petit, J. M., A. Morbidelli, and J. E. Chambers (2001), The primordial excitation and clearing of the asteroid belt, *Icarus*, *153*, 338–347, doi:10.1006/icar.2001.6702.

Poirier, J.-P. (2000), *Introduction to the Physics of the Earth's Interior*, 2nd ed., 312 pp., Cambridge Univ. Press, Cambridge, U. K.

Pollack, J. B., O. Hubickyj, P. Bodenheimer, J. J. Lissauer, M. Podolak, and Y. Greenzweig (1996), Formation of the giant planets by concurrent accretion of solids and gas, *Icarus*, *124*, 62–85, doi:10.1006/icar.1996.0190.

Popov, A. A., and S. V. Sobolev (2008), SLIM3D: A tool for three-dimensional thermomechanical modeling of lithospheric deformation with elasto-visco-plastic rheology, *Phys. Earth Planet. Inter.*, *171*, 55–75, doi:10.1016/j.pepi. 2008.03.007.

Ranalli, G. (1995), *Rheology of the Earth*, 2nd ed., 436 pp., Chapman and Hall, London.

Raymond, S. N., T. Quinn, and J. I. Lunine (2007), High-resolution simulations of the final assembly of Earth-like planets. 2. Water delivery and planetary habitability, *Astrobiology*, *7*, 66–84, doi:10.1089/ast.2006.06-0126.

Ricard, Y., O. Šrámek, and F. Dubuffet (2009), Runaway core-mantle segregation of terrestrial planets, *Earth Planet. Sci. Lett.*, *284*, 144–150, doi:10.1016/j.epsl.2009.04.021.

Rubie, D. C., H. J. Melosh, J. E. Reid, C. Liebske, and K. Righter (2003), Mechanisms of metal-silicate equilibration in the terrestrial magma ocean, *Earth Planet. Sci. Lett.*, *205*, 239–255, doi:10.1016/S0012-821X(02)01044-0.

Rubie, D. C., F. Nimmo, and H. J. Melosh (2007), Formation of the Earth's core, in *Treatise on Geophysics*, vol. 9, *Evolution of the Earth*, edited by D. J. Stevenson, pp. 51–90, Elsevier, Amsterdam.

Sahijpal, S., P. Soni, and G. Gupta (2007), Numerical simulations of the differentiation of accreting planetesimals with ^{26}Al and ^{60}Fe as the heat sources, *Meteorit. Planet. Sci.*, *42*, 1529–1548.

Samuel, H., and P. J. Tackley (2008), Dynamics of core formation and equilibration by negative diapirism, *Geochem. Geophys. Geosyst.*, *9*, Q06011, doi:10.1029/2007GC001896.

Sasaki, S., and K. Nakazawa (1986), Metal-silicate fractionation in the growing Earth: Energy source for the terrestrial magma ocean, *J. Geophys. Res.*, *91*, 9231–9238, doi:10.1029/JB091iB09p09231.

Sasaki, T., and Y. Abe (2007), Rayleigh-Taylor instability after giant impacts: Imperfect equilibration of the Hf-W system and its effect on the core formation time, *Earth Planets Space*, *59*, 1035–1045.

Schenk, O., and K. Gärtner (2004), Solving unsymmetric sparse systems of linear equations with PARDISO, *J. Future Gener. Comput. Syst.*, *20*, 475–487, doi:10.1016/j.future. 2003.07.011.

Schenk, O., and K. Gärtner (2006), On fast factorization pivoting methods for symmetric indefinite systems *Electron. Trans. Numer. Anal.*, *23*, 158–179.

Schmeling, H., et al. (2008), A benchmark comparison of spontaneous subduction models–towards a free surface, *Phys. Earth Planet. Inter.*, *171*, 198–223, doi:10.1016/ j.pepi.2008.06.028.

Scholz, C. H. (2002), *The Mechanics of Earthquakes and Faulting*, 2nd ed., 496 pp., Cambridge Univ. Press, New York.

Schubert, G., T. Spohn, and R. T. Reynolds (1986), Thermal histories, compositions and internal structures of the moons of the solar system, in *Satellites*, edited by J. A. Burns and M. S. Matthews, pp. 224–292, Arizona Univ. Press, Tucson.

Senshu, H., K. Kuramoto, and T. Matsui (2002), Thermal evolution of a growing Mars, *J. Geophys. Res.*, *107*(E12), 5118, doi:10.1029/2001JE001819.

Shewchuk, J. R. (1996), Engineering a 2D quality mesh generator and Delaunay triangulator, in *Applied Computational Geometry: Towards Geometric Engineering. Lecture Notes in Computer Science*, edited by M. C. Lin and D. Manocha, pp. 203–222, Springer, Berlin.

Sleep, N. (2000), Evolution of the mode of convection within terrestrial planets, *J. Geophys. Res.*, *105*, 17,563–17,578, doi:10.1029/2000JE001240.

Slezkin, A. (1955), *Dynamics of Viscous Incompressible Fluid* (in Russian), Gostekhizdat, Moscow.

Stevenson, D. J. (1981), Models of the Earth's core, *Science*, *214*, 611–619, doi:10.1126/science.214.4521.611.

Stevenson, D. J. (1990), Fluid dynamics of core formation, in *Origin of the Earth*, edited by H. E. Newsom and J. H. Jones, pp. 231–249, Oxford Univ. Press, New York.

Stevenson, D. J. (2001), Mars' core and magnetism, *Nature*, *412*, 214–219, doi:10.1038/35084155.

Stevenson, D. J. (2008), A planetary perspective on the deep Earth, *Nature*, *451*, 261–265, doi:10.1038/nature06582.

Taylor, S. R., and M. D. Norman (1990), Accretion of differentiated planetesimals to the Earth, in *Origin of the Earth*, edited by H. E. Newsom and J. H. Jones, pp. 29–43, Oxford Univ. Press, New York.

Terasaki, H., D. J. Frost, D. C. Rubie, and F. Langenhorst (2008), Percolative core formation in planetesimals, *Earth Planet. Sci. Lett.*, *273*, 132–137, doi:10.1016/j.epsl.2008. 06.019.

Tonks, W. B., and H. J. Melosh (1992), Core formation by giant impacts, *Icarus*, *100*, 326–346, doi:10.1016/0019-1035(92)90104-F.

Tonks, W. B., and H. J. Melosh (1993), Magma ocean formation due to giant impacts, *J. Geophys. Res.*, *98*(E3), 5319–5333, doi:10.1029/92JE02726.

Turcotte, D. L., and G. Schubert (2002), *Geodynamics*, 2nd ed., 456 pp., Cambridge Univ. Press, Cambridge, U. K.

Weinberg, R. F., and Y. Podladchikov (1994), Diapiric ascent of magmas through power law crust and mantle, *J. Geophys. Res.*, *99*, 9543–9559, doi:10.1029/93JB03461.

Weiss, B. P., J. S. Berdahl, L. Elkins-Tanton, S. Stanley, E. A. Lima, and L. Carporzen (2008), Magnetism on the angrite parent body and the early differentiation of planetesimals, *Science*, *322*, 713–716, doi:10.1126/science.1162459.

Wetherill, G. W. (1990), Formation of the Earth, *Annu. Rev. Earth Planet. Sci.*, *18*, 205–256, doi:10.1146/annurev.ea. 18.050190.001225.

Wetherill, G. W. (1992), An alternative model for the formation of the asteroids, *Icarus*, *100*, 307–325, doi:10.1016/ 0019-1035(92)90103-E.

Wood, B. J., J. Wade, and M. R. Kilburn (2008), Core formation and the oxidation state of the Earth: Additional constraints from Nb, V and Cr partitioning, *Geochim. Cosmochim. Acta*, *72*, 1415–1426, doi:10.1016/j.gca. 2007.11.036.

Yamazaki, D., and S. Karato (2001), Some mineral physics constraints on the rheology and geothermal structure of Earth's lower mantle, *Am. Mineral.*, *86*, 385–391.

Yoshino, T., M. J. Walter, and T. Katsura (2004), Connectivity of molten Fe alloy in peridotite based on in situ electrical conductivity measurements: Implications for core formation in terrestrial planets, *Earth Planet. Sci. Lett.*, *222*, 625–643, doi:10.1016/j.epsl.2004.03.010.

Yunker, M. L., and J. A. Van Orman (2007), Interdiffusion of solid iron and nickel at high pressure, *Earth Planet. Sci. Lett.*, *254*, 203–213, doi:10.1016/j.epsl.2006.11.036.

Ziethe, R., and T. Spohn (2007), Two-dimensional stokes flow around a heated cylinder: A possible application for diapirs in the mantle, *J. Geophys. Res.*, *112*, B09403, doi:10.1029/ 2006JB004789.